

Chromatic periodic activity down to 120 megahertz in a fast radio burst

<https://doi.org/10.1038/s41586-021-03724-8>

Received: 15 December 2020

Accepted: 14 June 2021

Published online: 25 August 2021

 Check for updates

Inés Pastor-Marazuela^{1,2}, Liam Connor^{1,2,3}, Joeri van Leeuwen^{1,2}✉, Yogesh Maan², Sander ter Veen², Anna Bilous², Leon Oostrum^{1,2,4}, Emily Petroff¹, Samayra Straal^{5,6}, Dany Vohl², Jisk Attema⁴, Oliver M. Boersma^{1,2}, Eric Kooistra², Daniel van der Schuur², Alessio Sciacco⁴, Roy Smits², Elizabeth A. K. Adams^{2,7}, Björn Adebarh⁸, W. J. G. de Blok^{2,7,9}, Arthur H. W. M. Coolen², Sieds Damstra², Helga Dénes², Kelley M. Hess^{2,7}, Thijs van der Hulst⁷, Boudewijn Hut², V. Marianna Ivashina¹⁰, Alexander Kutkin^{2,11}, G. Marcel Loose², Danielle M. Lucero¹², Ágnes Mika², Vanessa A. Moss^{2,13,14}, Henk Mulder², Menno J. Norden², Tom Oosterloo^{2,7}, Emanuela Orrú², Mark Ruiter² & Stefan J. Wijnholds²

Fast radio bursts (FRBs) are extragalactic astrophysical transients¹ whose brightness requires emitters that are highly energetic yet compact enough to produce the short, millisecond-duration bursts. FRBs have thus far been detected at frequencies from 8 gigahertz (ref. ²) down to 300 megahertz (ref. ³), but lower-frequency emission has remained elusive. Some FRBs repeat^{4–6}, and one of the most frequently detected, FRB 20180916B⁷, has a periodicity cycle of 16.35 days (ref. ⁸). Using simultaneous radio data spanning a wide range of wavelengths (a factor of more than 10), here we show that FRB 20180916B emits down to 120 megahertz, and that its activity window is frequency dependent (that is, chromatic). The window is both narrower and earlier at higher frequencies. Binary wind interaction models predict a wider window at higher frequencies, the opposite of our observations. Our full-cycle coverage shows that the 16.3-day periodicity is not aliased. We establish that low-frequency FRB emission can escape the local medium. For bursts of the same fluence, FRB 20180916B is more active below 200 megahertz than at 1.4 gigahertz. Combining our results with previous upper limits on the all-sky FRB rate at 150 megahertz, we find there are 3–450 FRBs in the sky per day above 50 Jy ms. Our chromatic results strongly disfavour scenarios in which absorption from strong stellar winds causes FRB periodicity. We demonstrate that some FRBs are found in ‘clean’ environments that do not absorb or scatter low-frequency radiation.

We observed FRB 20180916B (also called FRB180916.J0158+65) simultaneously with the Westerbork/Apertif and LOFAR radio telescopes, and detected multiple bursts with both facilities. Curiously, none occurred simultaneously in both frequency bands. The Apertif Radio Transient System⁹ observed between 1,220 MHz and 1,520 MHz for 388.4 h, covering seven activity cycles. We recorded 48.3 h of simultaneous LOFAR¹⁰ observations between 110 MHz and 190 MHz, during the predicted peaks of three cycles. The LOFAR data are public, and are being analysed independently¹¹. We detected 54 bursts with Apertif and 9 with LOFAR (Fig. 1).

No previous low-frequency searches, either all-sky^{12,13} or targeting known repeaters³, detected any FRBs. Those strict limits on emission below 300 MHz fuelled FRB theories in which local free–free absorption or strong intervening scattering was required. The nine LOFAR bursts

presented here (Fig. 2, Extended Data Table 1) are the first FRB detections in this low-frequency range. All had simultaneous Apertif coverage, but none were detected there above our flux density limit of 1.7 Jy.

Notably, FRB 20180916B emits over 10× more bursts of the same fluence at 150 MHz than at 1.4 GHz (Extended Data Fig. 1). Our detections allow bounded FRB all-sky rate constraints to be determined below 200 MHz. A lower limit is obtained by assuming only FRB 20180916B is visible in the low-frequency radio sky. Combining this with previously published upper limits, we infer 3–450 bursts over the whole sky per day above 50 Jy ms. A Euclidean fluence scaling then predicts 90–14,000 bursts over the whole sky per day above 5 Jy ms at 150 MHz, which is promising for future low-frequency surveys.

The LOFAR bursts (Fig. 2) are dominated by a sharp rise plus a scattering tail. The scattering timescale $\tau_{sc} = 46 \pm 10$ ms at 150 MHz scales with

¹Anton Pannekoek Institute, University of Amsterdam, Amsterdam, The Netherlands. ²ASTRON, the Netherlands Institute for Radio Astronomy, Dwingeloo, The Netherlands. ³Cahill Center for Astronomy, California Institute of Technology, Pasadena, CA, USA. ⁴Netherlands eScience Center, Amsterdam, The Netherlands. ⁵NYU Abu Dhabi, Abu Dhabi, United Arab Emirates. ⁶Center for Astro, Particle, and Planetary Physics (CAP³), NYU Abu Dhabi, Abu Dhabi, United Arab Emirates. ⁷Kapteyn Astronomical Institute, Groningen, The Netherlands. ⁸Astronomisches Institut der Ruhr-Universität Bochum (AIRUB), Bochum, Germany. ⁹Department of Astronomy, University of Cape Town, Rondebosch, South Africa. ¹⁰Department of Electrical Engineering, Chalmers University of Technology, Gothenburg, Sweden. ¹¹Astro Space Center of Lebedev Physical Institute, Moscow, Russia. ¹²Department of Physics, Virginia Polytechnic Institute and State University, Blacksburg, VA, USA. ¹³CSIRO Astronomy and Space Science, Australia Telescope National Facility, Epping, New South Wales, Australia. ¹⁴Sydney Institute for Astronomy, School of Physics, University of Sydney, Sydney, New South Wales, Australia. ✉e-mail: leeuwen@astron.nl

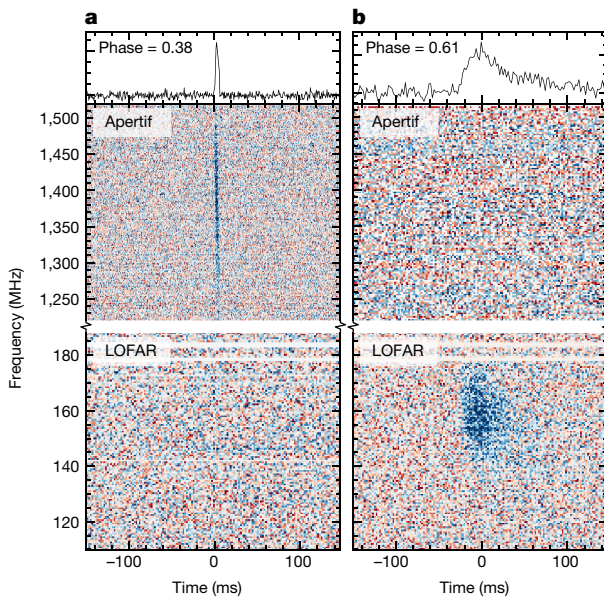


Fig. 1 | Two bursts at different phases. **a, b,** The bursts appear in either the Apertif (middle) or LOFAR (bottom) bands of the dynamic spectra. Top, pulse profile of each burst, the ordinate denoting flux density in arbitrary units. **a,** Burst A13, detected at activity phase 0.38, is detected only at 1.4 GHz, with no emission below 190 MHz. **b,** Burst L06 occurred at phase 0.61 and is only detected by LOFAR.

frequency ν as $\tau_{\text{sc}} \propto \nu^{-4.2 \pm 1.1}$, consistent with the approximately 60-kHz scintillation seen at 1.7 GHz (ref. ¹⁴). The scattering may explain why none of the millisecond-duration frequency–time subcomponents seen at higher frequencies¹⁵ are visible (Fig. 2). The pulse broadening is consistent with Galactic scattering¹⁶, and no host galaxy contribution is required. The local environment notably scatters the FRB by $\lesssim 7 \mu\text{s}$ at 1.4 GHz. The dispersion measure (DM) of the LOFAR bursts, $\text{DM}_{\text{LOFAR}} = 349.00 \pm 0.02 \text{ pc cm}^{-3}$ (Methods), exceeds measurements taken 10 months earlier at 1.7 GHz (ref. ¹⁴) by about 0.24 pc cm^{-3} . We interpret this excess, again, as the presence of unresolved time–frequency subcomponents.

For bursts L01 and L07, FRB 20180916B emits down to 120 MHz (Fig. 2). We cannot confidently rule out the presence of emission below 120 MHz, given the reduced LOFAR sensitivity there. Our low-frequency detections show that free–free absorption and induced Compton scattering do not substantially affect burst propagation for this source. Combined with the small local rotation and DM contribution, and the lack of temporal scattering, these detections show that some FRBs reside in clean environments, a prerequisite for certain FRB applications to cosmology¹⁷.

In our Apertif campaign, we detected 54 bursts (Extended Data Figs. 2, 3, and Extended Data Table 2). LOFAR co-observed 10 of these, but detected none above a 30 Jy ms fluence. All 26 bursts for which polarization data were recorded are approximately 100% linearly polarized. The polarization position angle (PA) is constant within single bursts, and relatively flat both over activity phase and between cycles. This observation can be used to constrain the FRB emission mechanism and the origin of periodic activity.

After dedispersion by maximizing the burst structure^{2,15} (Methods), a large fraction of 1.4-GHz bursts show multiple subcomponents that

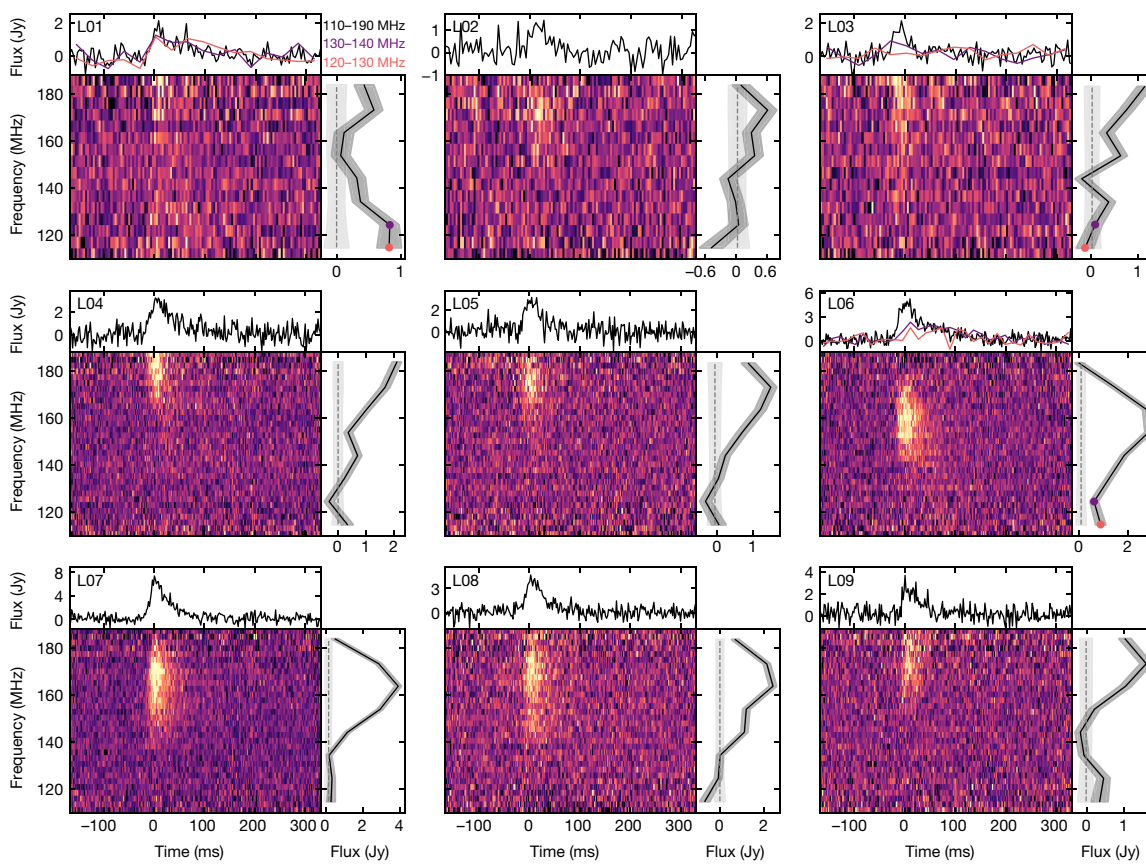


Fig. 2 | The nine LOFAR bursts. For each burst (L01–L09) we show the calibrated pulse profile (top), the dedispersed dynamic spectrum (main panel), and the spectrum (right). Bursts L01, L03 and L06 show emission below 140 MHz, and those sub-band profiles are plotted in purple and pink.

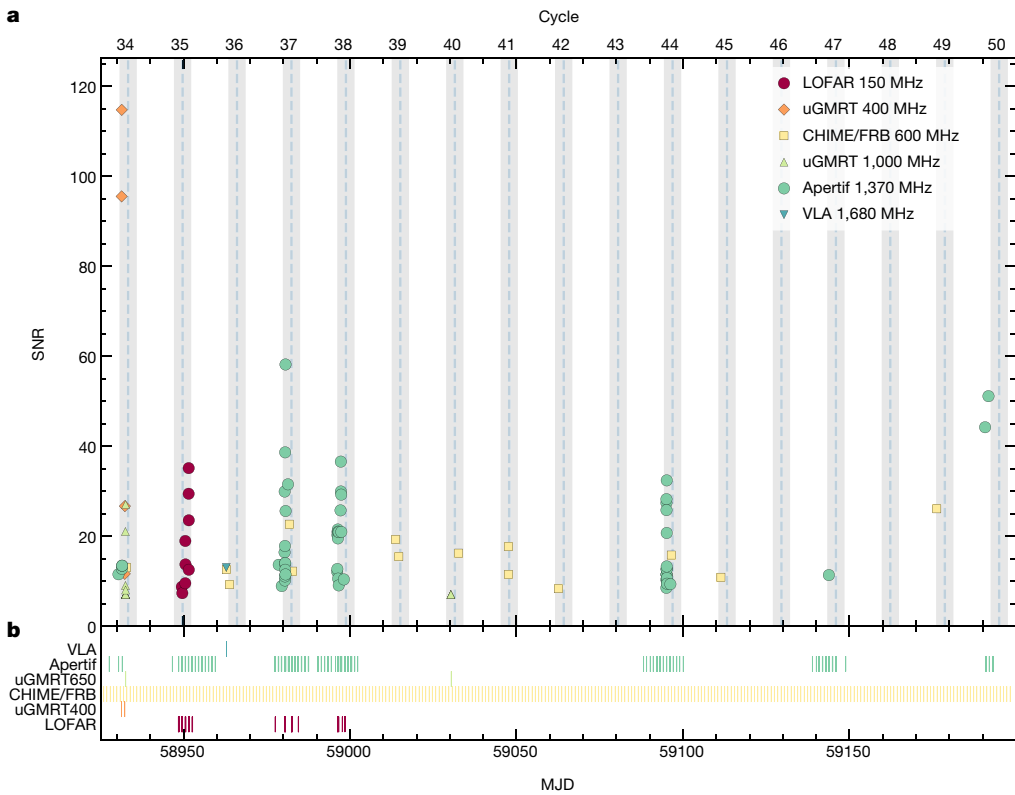


Fig. 3 | Coverage and detection times. The detection signal-to-noise ratios (SNRs) (a) and the observation epochs for our campaigns and other instruments^{20,29,30} (b) are plotted as a function of modified Julian date (MJD)

(bottom axis) and CHIME/FRB cycle number (top axis). Here and in subsequent figures, Apertif is shown in green and LOFAR in crimson. The predicted 16.35-day-period active days are marked in grey.

drift downward in frequency (Extended Data Fig. 8). This phenomenon seems common among repeating FRBs^{2,5,7,15}. For FRB 20180916B, drift rates had been estimated below 800 MHz, with $v = -4.2 \pm 0.4$ MHz ms⁻¹ at 400 MHz (ref.³) and -21 ± 3 MHz ms⁻¹ at 600 MHz (ref.¹⁸). The average drift rate we measure at 1,370 MHz, of -39 ± 7 MHz ms⁻¹, is nine times larger than at 400 MHz. The average drift rate values evolve linearly with frequency, as in FRB 20121102A¹⁹.

Our coverage (Fig. 3) with LOFAR focused on peak days to maximize the detection probability, and Apertif observations spanned the entire 16.35-day activity cycle, to find or rule out any potential aliasing. The possibility of an aliased period remained, mostly driven by the brevity and daily cadence of the CHIME/FRB exposures (Extended Data Fig. 4). From periodograms²⁰ based on our and previously published detections, we confirm the best period is $16.29^{+0.15}_{-0.17}$ days. This period minimizes the activity width fraction for bursts detected between 110 MHz and 1,765 MHz. We also searched for short periodicities within all our observations, but found none between 1 ms and 80 s.

Apertif bursts were found in six out of seven cycles. The LOFAR bursts occurred in a single cycle, with no 1.4-GHz detections, probably because Apertif observed at relatively late phase. Most Apertif bursts arrive before CHIME/FRB's activity peak day, while LOFAR bursts arrive after. Although previous observations of FRB 20180916B had hinted at a frequency dependent activity window⁸, the scarcity of non-CHIME/FRB bursts prevented precise characterization of the dependence of the activity window on frequency, its chromaticity. Using the Apertif, CHIME/FRB and LOFAR burst samples, we have evaluated the 1,400-MHz, 600-MHz and 150-MHz activity windows. Folding the burst arrivals at the best period of 16.29 days (Fig. 4, Methods), we determine the burst rate to phase relationship for each instrument. We find the activity window is narrower and peaks earlier at 1.4 GHz than at 600 MHz. The peak at Apertif occurs about 0.7 days before CHIME/FRB, and the burst window is half as wide. LOFAR activity peaks

approximately 2 days later than CHIME/FRB, but the lower number of detections and the uneven phase coverage prevent a better activity window width estimate. Thus, the overall FRB activity moves to ever lower frequencies throughout the phase. The similarity with the much-shorter-timescale downward drifting emission within individual bursts is notable. We evaluated the likelihood of the bursts being drawn from the same distribution, taking into account the survey strategy. We are confident at the 4σ level that the Apertif and LOFAR bursts do not follow the same distribution. The CHIME/FRB and Apertif burst

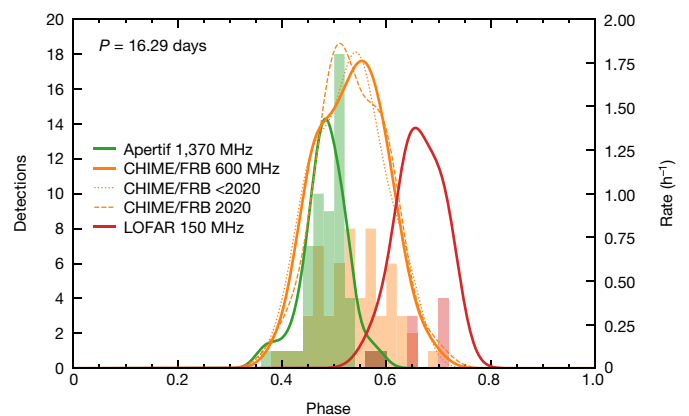


Fig. 4 | Frequency dependence of the FRB 20180916B activity windows. Chromatic burst activity windows versus phase for Apertif (green), CHIME/FRB (orange) and LOFAR (red) are shown, for the best-fit period of 16.29 days. The histograms represent the detections, the solid lines are the rates obtained with kernel density estimates (KDEs). The KDEs for the pre-2020 and 2020 subsets of CHIME/FRB bursts (dotted and dashed lines) establish that the wider CHIME activity window is not due to a longer time baseline.

distributions, too, are different at 4σ confidence (Methods, Extended Data Fig. 5).

The discovery of periodic activity in FRB 20180916B, and a subsequent report of 160-day periodicity in FRB 20121102A²¹, led to many new FRB models with periodic aspects. One category places the engine of FRB 20180916B (a pulsar or magnetar) in a binary system with an orbital period of about 16 days. Free-free absorption in the wind from the companion (a massive star or another neutron star^{22,23}) obscures the coherent radio emission from the engine for most of the orbit. Such models predict frequency-dependent, chromatic activity windows, but as the absorption effects are stronger at low frequencies, the phase windows should be narrower there. We observe the opposite. Additionally, these models predict a DM evolution due to the dynamic absorption column, and a low-frequency cutoff. Our observations of a smaller phase range at higher frequencies, constant DM, and emission down to 120 MHz challenge all three predictions of these models. With the chromatic data presented in this work, simple absorptive binary wind models are highly disfavoured as an explanation for the periodicity of FRB 20180916B.

In other models, the periodic activity follows from magnetar precession. The precession is either free for isolated magnetars^{24,25} or forced from, for example, a fallback disk²⁶. Precession models predict a second, shorter periodicity, from the neutron star rotation itself. We find no such intra-window periodicity. The spin noise, pulse profile instability, or dephased beams expected in young magnetars could, however, conceal this signal. FRBs produced from a rotating neutron-star beam should show a PA sweep²⁵. We instead observe a flat PA. Furthermore, free precession models typically require young, hot and highly active magnetars that may still be embedded in their birth environment. The limits we set on local scattering, absorption and DM variation suggest, however, that FRB 20180916B is no longer surrounded by a dense supernova remnant and that any remaining magnetar wind is not hampering radio propagation.

A precessing magnetar could also produce the required periodic coherent radio emission farther out. In synchrotron maser shock models²⁷, a magnetar flare causes an ultra-relativistic shock when colliding with the neighbouring medium. The FRB emission is produced in this magnetized shock. This model predicts the flat, constant intra-burst PAs we observe, perpendicular to the upstream magnetic field of the surrounding material. But it is not clear whether such models can power emitters as prolific as FRB 20180916B and FRB 20121102A. The absence of short periodicity and DM variation with phase is consistent with the ultra-long-period magnetar scenario²⁸. That model, however, requires expelling enough angular momentum to produce a period that is five orders of magnitude larger than any definitively-known neutron star rotation period.

Online content

Any methods, additional references, Nature Research reporting summaries, source data, extended data, supplementary information, acknowledgements, peer review information; details of author contributions and competing interests; and statements of data and code availability are available at <https://doi.org/10.1038/s41586-021-03724-8>.

1. Lorimer, D. R., Bailes, M., McLaughlin, M. A., Narkevic, D. J. & Crawford, F. A bright millisecond radio burst of extragalactic origin. *Science* **318**, 777–780 (2007).
2. Gajjar, V. et al. Highest-frequency detection of FRB 121102 at 4–8 GHz using the breakthrough listen digital backend at the Green Bank Telescope. *Astrophys. J.* **863**, 2 (2018).
3. Chawla, P. et al. Detection of repeating FRB 180916.J0158+65 down to frequencies of 300 MHz. *Astrophys. J.* **896**, L41 (2020).
4. Spitler, L. G. et al. A repeating fast radio burst. *Nature* **531**, 202–205 (2016).
5. The CHIME/FRB Collaboration. A second source of repeating fast radio bursts. *Nature* **566**, 235–238 (2019).
6. Fonseca, E. et al. Nine new repeating fast radio burst sources from CHIME/FRB. *Astrophys. J.* **891**, L6 (2020).
7. The CHIME/FRB Collaboration et al. CHIME/FRB detection of eight new repeating fast radio burst sources. *Astrophys. J.* **885**, L24 (2019).
8. The CHIME/FRB Collaboration. Periodic activity from a fast radio burst source. *Nature* **582**, 351–355 (2020).
9. Maan, Y. & van Leeuwen, J. Real-time searches for fast transients with Apertif and LOFAR. In *IEEE Proc. URSI GASS* <https://doi.org/10.23919/URSIGASS.2017.8105320> (IEEE, 2017).
10. Stappers, B. W. et al. Observing pulsars and fast transients with LOFAR. *Astron. Astrophys.* **530**, A80 (2011).
11. Pleunis, Z. et al. LOFAR detection of 110–188 MHz emission and frequency-dependent activity from FRB 20180916B. *Astrophys. J. Lett.* **911**, L3 (2021).
12. Coenen, T. et al. The LOFAR pilot surveys for pulsars and fast radio transients. *Astron. Astrophys.* **570**, A60 (2014).
13. Karastergiou, A. et al. Limits on fast radio bursts at 145 MHz with ARTEMIS, a real-time software backend. *Mon. Not. R. Astron. Soc.* **452**, 1254–1262 (2015).
14. Marcote, B. et al. A repeating fast radio burst source localized to a nearby spiral galaxy. *Nature* **577**, 190–194 (2020).
15. Hessels, J. W. T. et al. FRB 121102 bursts show complex time-frequency structure. *Astrophys. J.* **876**, L23 (2019).
16. Cordes, J. M. & Lazio, T. J. W. NE2001.I. A new model for the Galactic distribution of free electrons and its fluctuations. Preprint at <http://arXiv.org/abs/astro-ph/0207156> (2003).
17. McQuinn, M. Locating the “missing” baryons with extragalactic dispersion measure estimates. *Astrophys. J.* **780**, L33 (2014).
18. Chamma, M. A., Rajabi, F., Wyenberg, C. M., Mathews, A. & Houde, M. Evidence of a shared law between sources of repeating fast radio bursts. Preprint at <http://arXiv.org/abs/2010.14041> (2020).
19. Josephy, A. et al. CHIME/FRB detection of the original repeating fast radio burst source FRB 121102. *Astrophys. J.* **882**, L18 (2019).
20. Aggarwal, K. et al. VLA/realfast detection of burst from FRB180916.J0158+65 and tests for periodic activity. *Res. Notes AAS* **4**, 94 (2020).
21. Rajwade, K. M. et al. Possible periodic activity in the repeating FRB 121102. *Mon. Not. R. Astron. Soc.* **495**, 3551–3558 (2020).
22. Lyutikov, M., Barkov, M. & Giannios, D. FRB-periodicity: mild pulsar in tight O/B-star binary. *Astrophys. J.* **893**, L39 (2020).
23. Ioka, K. & Zhang, B. A binary comb model for periodic fast radio bursts. *Astrophys. J.* **893**, L26 (2020).
24. Levin, Y., Beloborodov, A. M. & Bransgrove, A. Precessing flaring magnetar as a source of repeating FRB 180916.J0158+65. *Astrophys. J.* **895**, L30 (2020).
25. Zanazzi, J. J. & Lai, D. Periodic fast radio bursts with neutron star free/radiative precession. *Astrophys. J.* **892**, L15 (2020).
26. Tong, H., Wang, W. & Wang, H. G. Periodicity in fast radio bursts due to forced precession by a fallback disk. *Res. Astron. Astrophys.* **20**, 142 (2020).
27. Metzger, B. D., Margalit, B. & Sironi, L. Fast radio bursts as synchrotron maser emission from decelerating relativistic blast waves. *Mon. Not. R. Astron. Soc.* **485**, 4091–4106 (2019).
28. Beniamini, P., Wadiasingh, Z. & Metzger, B. D. Periodicity in recurrent fast radio bursts and the origin of ultra long period magnetars. *Mon. Not. R. Astron. Soc.* **496**, 3390–3401 (2020).
29. Sand, K. R. et al. Low-frequency detection of FRB180916 with the uGMRT. *Astron. Telegr.* **13781** (2020).
30. Marthi, V. R. et al. Detection of 15 bursts from FRB 180916.J0158+65 with the uGMRT. *Mon. Not. R. Astron. Soc. Lett.* **499**, L16–L20 (2020).

Publisher's note Springer Nature remains neutral with regard to jurisdictional claims in published maps and institutional affiliations.

© The Author(s), under exclusive licence to Springer Nature Limited 2021

Methods

Observations and burst search

Apertif. The Westerbork Synthesis Radio Telescope (WSRT) is a radio interferometer located in Drenthe, The Netherlands, consisting of twelve 25-m dishes in which a new system called Apertif (Aperture Tile in Focus) has recently been installed. Single receivers have been replaced by phased array feeds, increasing its field of view to about 8.7 square degrees^{31,32}. Apertif can work in time-domain observing mode to search for new FRBs³³ and follow-up known ones³⁴ using eight of the WSRT dishes. This capability is provided by a new backend, ARTS (the Apertif Radio Transient System^{9,35,36}). ARTS covers the full Apertif field-of-view with up to 3,000 tied-array beams, each with a typical half-power size of 25' by 25''. In real-time FRB searches, the system records Stokes I data at a central frequency of 1,370 MHz and a 300-MHz bandwidth with 81.92 μ s and 195 kHz time and frequency resolution. The data are then searched in near-real time with our burst search software AMBER^{37–39} and post-processing software DARC⁴⁰. Raw FRB candidates are then filtered by a machine learning algorithm that assigns a probability of the candidate being of true astrophysical origin⁴¹ and later checked by human eyes. When AMBER identifies an FRB candidate with a duration <10 ms, a signal-to-noise ratio (S/N) >10 and a dispersion measure (DM) 20% larger than the expected Milky Way contribution to the DM in the pointing direction according to the YMW16 model⁴², the full Stokes IQUV data of the candidate is saved. When following up known sources, the system also stores Stokes IQUV for any candidate with S/N >10 and a DM within 5 pc cm⁻³ of the source DM.

We carried out observations of FRB 20180916B with Apertif, resulting in 388.4 h on source. The observations covered seven cycles of the predicted 16.35-day activity period of FRB 20180916B, and the exposure times are visualized in Fig. 3b. The observations of the three activity cycles after our first detection (numbered 35, 37 and 38) ranged over the whole activity phase instead of only at the predicted active days to rule out or confirm any potential aliasing of the period⁸. The later observations were scheduled at the confirmed activity peak days.

For 165 out of 388 observing hours, the high-resolution data were kept for a deeper offline search with PRESTO⁴³. After masking channels known to be affected by radio frequency interference (RFI) with rfifind, the data were dedispersed to DMs between 310 pc cm⁻³ and 397 pc cm⁻³ in steps of 0.3 pc cm⁻³. Each time series was then searched for single pulses with S/N > 8 and width <100 ms with single_pulse_search.py. After clustering the candidates in DM and time, the candidate with the highest S/N in each cluster was visualized and inspected by eye. A small fraction of the data were strongly affected by RFI, mainly in cycle 44 (as numbered in Fig. 3) during 2020 September 3 and 4. These data were cleaned with RFIClean (<https://github.com/ymaan4/rficlean>) and RFI was further masked with rfifind. A large fraction of channels was masked completely. Hence we cannot exclude the presence of faint or narrowband bursts that would have been above our sensitivity threshold without RFI.

In addition to the single pulse search, we searched the data for periodic signals with periods between 0.1 ms and 1 s using PRESTO's accelsearch. To account for any drift in the pulse frequency due to acceleration of the source in a putative orbit, an acceleration search was performed with a maximum Fourier-drift parameter of $z=200$, corresponding to a maximum line-of-sight acceleration of 0.5 m s⁻² for a periodicity of 1 ms and the typical observation duration of 3 h. The implicit assumption of constant acceleration holds as long as the orbit is longer than about 30 h. All candidates were inspected visually.

LOFAR. The LOw Frequency ARray (LOFAR^{10,44}) is an interferometric array of radio telescopes. Most LOFAR stations are located across The Netherlands, with a core in Drenthe, while 14 are distributed in neighbouring countries to increase its spatial resolution. The observations presented here used between 18 and 23 core (Dutch) stations, and used

coherent Stokes mode at a time resolution of 983.04 μ s and a frequency resolution of 3.052 kHz. Most data, including all detections, were recorded in intensity only (Stokes I). Data from 2020 May 27–29 were recorded in full polarization (Stokes IQUV).

LOFAR was used to obtain 48.3 h of beam-formed data between 110 MHz and 188 MHz, simultaneously with Apertif observations. LOFAR observations were taken at the predicted active days to increase the chances of detecting bursts that are broad band from 1.4 GHz to 150 MHz at both telescopes.

The observations were taken during commissioning of the transient buffer boards at LOFAR. In this observing mode, up to five dispersed seconds of raw sub-band data can be saved when a trigger is sent from another instrument. During the simultaneous Apertif–LOFAR observations, if AMBER detected a burst with S/N > 10 and a DM within five units of 349.2 pc cm⁻³, Apertif sent a trigger to LOFAR. The dispersive delay of 40 s between 1,220 MHz, the bottom of the Apertif band, and 188 MHz, the top of the band for the LOFAR High Band Antenna, gives enough time for the pipeline to find the candidate and send the alert, so that LOFAR can freeze the raw data in time.

The offline search for FRBs and periodic emission used PRESTO. The data were first sub-banded using Sigproc. In this process, every 25 consecutive channels were dedispersed using a DM of 349.5 pc cm⁻³ and averaged together, resulting in 1,024 sub-bands across the full 78.1 MHz bandwidth. Strong periodic RFI and other interference were mitigated using RFIClean⁴⁵, and any remaining RFI were subsequently masked using PRESTO's rfifind. The data were then dedispersed to DMs between 342 pc cm⁻³ and 358 pc cm⁻³ in steps of 0.03 pc cm⁻³. Each dedispersed time series was searched for single pulses with S/N > 7 and pulse width <250 ms using PRESTO's single_pulse_search.py. Similarly to the offline search of the Apertif data, the candidates were clustered in DM and time, and the candidate with the highest S/N in each cluster was visualized and examined by eye. Each of the dedispersed time series was also subjected to a periodicity search using PRESTO's accelsearch, with a maximum Fourier-drift parameter of $z=128$. This value implies that, for an observing duration of 1 h, we have searched for average accelerations of about 2.96 m s⁻² and 296 m s⁻² of 1,000 Hz and 10 Hz signals, respectively. We note that our periodicity search is not sensitive to periods shorter than a few tens of milliseconds owing to significant scatter-broadening at the LOFAR frequencies. For each observation, all the candidates with periods up to 80 s were folded and the corresponding diagnostic plots were examined by eye.

Data analysis

Detected bursts. During our observing campaign, we detected a total of 63 bursts, 54 with Apertif and 9 with LOFAR. None of these detections took place simultaneously at both instruments. Figure 3a shows the S/N of each detection as a function of modified Julian date (MJD). It includes the detections by other instruments during the same time span for comparison, and the observation times in Fig. 3b. The predicted activity days for a period of 16.35 days are illustrated as shaded regions to guide the eye, and the cycle numbers since the first CHIME/FRB detection are indicated on top.

Bursts detected with Apertif. We detected a total of 54 bursts with an S/N above 8 in 388.4 h of observations with Apertif. All Apertif bursts are given an identifier AXX, where XX is the burst number ordered by time of arrival within the Apertif bursts, from A01 to A54. Twenty-six of those bursts triggered a dump of the full-Stokes data. Eight of the bursts were not detected in real time, but in the later search of the filterbank observations with PRESTO. The number of IQUV triggers during cycle 44 is lower owing to the incremented RFI environment that triggered IQUV dumps on RFI and avoided saving IQUV data on later real bursts. Extended Data Table 2 summarizes the main properties of the detected bursts. All detections took place in six out of the seven predicted activity cycles that our observations covered. In spite of

Article

observing FRB 20180916B during five days centred at the predicted Apertif peak day during cycle 47, only one burst was detected, revealing that the burst rate can fluctuate from cycle to cycle. Extended Data Figs. 2 and 3 show the dynamic spectra and pulse profile of all bursts. Additionally, Stokes L and V are plotted for the bursts with full-Stokes data, together with the polarization position angle (PA).

As shown in Fig. 3, all Apertif bursts were detected in a four-day window before the predicted peak day of the corresponding activity cycle, with none of the detections happening after the peak. There were no detections outside a six-day activity window, even though they were largely covered by our observations. The late start of the observations around MJD 58950 with respect to the beginning of the predicted activity window could explain the non-detections in that cycle. However, the lack of emission at 1.4 GHz during that cycle cannot be discarded. After our detections and non-detections during the first four cycles, we refined the expected active window time at 1.4 GHz and scheduled the observations of the last three cycles accordingly, in five-day windows centred at the predicted Apertif peak day. The detected bursts present a large variety of properties. Some display a single component, others show rich time-frequency structure with up to five components.

To estimate the fluence of all Apertif bursts, we obtained the mean pulse profiles using 21-ms time windows centred at each pulse's peak. This window duration is larger than the widest burst, except for A53 where a 42-ms window was needed to cover the whole burst duration. We normalized each pulse profile by the standard deviation of an off-burst region to convert the time series into SNR units. We determined the system-equivalent flux density (SEFD) by performing drift scans of the calibrator sources 3C147 and 3C286 whose flux densities are known⁴⁶. Next we applied the radiometer equation^{47,48} to convert the pulse profile into flux units (Jy) using the SEFD, and integrated over the 21-ms or 42-ms time windows to obtain the fluence of each burst (Jy ms). We applied this technique to account for the burst structure. We assume 20% errors on the fluence based on the instability of the system over several days of observations.

The cumulative distribution function (CDF) of the fluences of the Apertif bursts, presented in Extended Data Fig. 1, can be fitted to a broken power law with two turnovers. By applying a least squares minimization technique and assuming Poissonian errors on the rate, we find the break fluences to be located at 3.2 ± 0.2 Jy ms and 7.8 ± 0.4 Jy ms. For bursts with $S/N > 10$ displaying the typical burst width of 2 ms, our fluence completeness threshold is about 1.7 Jy ms. The full range of widths for pulses near our S/N detection limit (Extended Data Figs. 2, 3) is 1–5 ms, which leads to a fluence range of 1–3 Jy ms (Extended Data Table 2). The lower-fluence turnover falls right above this range and we will thus assume that it is due to the Apertif sensitivity. The 7.8 Jy ms turnover is, however, above our completeness threshold and cannot be due to instrumental effects. CHIME/FRB bursts have been observed to show a turnover at 5.3 Jy ms that was associated with the sensitivity of the instrument⁸. The potential presence of a turnover at 7.8 Jy ms intrinsic to the fluence distribution of FRB 20180916B could have been concealed by the sensitivity turnover. Each segment of the broken power law of the CDF follows $R(>F) \propto F^\beta$, in which R is the rate (in h^{-1}), F the fluence (in Jy ms) and β the power-law index. For $F > 7.8$ Jy ms, we get $\beta = -1.4 \pm 0.1$. This index is consistent with the CDF of CHIME/FRB bursts, where $\alpha = \beta - 1 \approx -2.3$ is obtained. For bursts with $3.2 \text{ Jy ms} < F < 7.8 \text{ Jy ms}$ we get $\beta = -0.7 \pm 0.1$, and for $F < 3.2$ Jy ms we get $\beta = -0.2 \pm 0.1$. All errors represent the standard deviation of the fitted parameters.

Bursts detected with LOFAR. We detected a total of nine LOFAR bursts above a S/N of 7 in about 48 h of observations. The bursts occurred on 10, 11 and 12 April 2020. Each burst is given an identifier LYY, where YY is the burst number ordered by time of arrival within LOFAR bursts, from L01 to L09. Extended Data Table 1 summarizes the properties of these bursts.

As shown in Fig. 3, all detections took place on the same predicted activity cycle in which there were no Apertif detections (cycle 35). The observations where the detections took place were performed in coherently beamformed Stokes I mode. Excepting the first two, all bursts arrived after the predicted peak day. There were thus no simultaneous bursts at 1.4 GHz and 150 MHz in the beamformed data or the transient buffer boards. From the dynamic spectra and pulse profiles displayed in Fig. 2, there is no evidence of complex, resolved time-frequency structure. Nevertheless, a scattering tail is manifest in the pulse profiles of the brightest bursts. We will characterize the scattering timescale below. While the tail of burst L06 in Fig. 1 appears to plateau 25 ms after the main peak, hinting at a second sub-burst, a fit for multiple scattered bursts did not confidently identify a second component.

Generally, the LOFAR-detected bursts are brightest in the top of the band (Fig. 2). Over the almost 2:1 ratio of frequency from the top of the band to the bottom, most bursts gradually become less bright. Although some previous targeted LOFAR FRB searches used wide bandwidths⁴⁹, most large-area searches were carried out in the lower part of the band, for example, 119–151 MHz (refs. ^{12,50}) where the LOFAR beams are both more sensitive and larger, maximizing the survey speed. Taking the sky background and the telescope sensitivity into account, a burst of the same fluence would have been detected with a 10% higher signal-to-noise ratio in that 32 MHz band from 119 MHz to 151 MHz, than in same bandwidth at the top of the band, from 158 MHz to 190 MHz. The behaviour we see here was probably a factor in the earlier lack of detections.

The detections reported here already demonstrate there is no low-frequency cutoff above the LOFAR band. The individual bursts and the stacked profile (Extended Data Fig. 6) also do not show a clear cutoff within the band. Two of the bursts (L01, L06) emit down to at least 120 MHz and thus cover the entire frequency range. These LOFAR burst spectra are compared to the telescope sensitivity limits in the right panels of Fig. 2. We averaged the flux densities for the bursts over fixed $[-50, +150]$ ms windows around the burst peak (dashed grey lines in the Fig. 2 right panels), and contrast these with the off-burst windows (solid black lines in the same panels), given the $\pm 1\sigma$ telescope sensitivity limits (grey contours). These limits are calculated as the standard deviation of 3-s off-burst intervals, scaled to the 200-ms on-burst window. The LOFAR minimum detectable flux varies over the recorded band; it is higher at the band edges. The response (light grey contours) is relatively flat compared to the burst brightness. Seemingly significant negative pulse flux densities at low frequencies in, for example, L02 and L08 were caused by slowly varying, low-level residual RFI that affected the baseline subtraction. Nevertheless, bursts L01 and L06 clearly show emission above the noise level, at the lower edge of the LOFAR band.

Furthermore, if we follow burst L06 from 150 MHz to 120 MHz in decreasing frequency, the emission is ever more delayed with respect to the onset of the peak (Figs. 1, 2). Such behaviour suggests unresolved time-frequency downward drift in the tail of the pulse. From this we conclude that the decrease in pulse peak brightness could be intrinsic, and is not due to a cutoff by intervening material. Bursts L04 and L05 show a similar hint of a delayed tail, at slightly higher frequencies.

The LOFAR flux density scale was derived from the radiometer equation, using information about frequency-dependent antenna and sky temperatures, models of telescope gain (frequency- and direction-dependent), number of performing stations/tiles, and RFI environment. It also takes the observing bandwidth, integration time, and number of summed polarizations into account. We estimate that imperfect knowledge of the system parameters introduces a 50% systematic uncertainty on the band integrated flux. The calibration procedure and flux uncertainty estimates are detailed in the LOFAR censuses of millisecond⁵¹ and normal⁵² pulsars.

Extended Data Figure 1 shows the CDF of LOFAR bursts. It can be fitted to a broken power law with the break fluence located at 104 ± 12 Jy ms. This fluence falls well within our LOFAR sensitivity limits, and we thus

attribute the break to our completeness level. The power-law index of bursts with $F > 104$ Jy ms is $\Gamma = -1.5 \pm 0.2$, consistent with the Apertif and the CHIME/FRB power-law indices. However, the burst rate at the same fluence is two orders of magnitude larger for LOFAR bursts than for Apertif bursts. The power-law index for bursts with $F < 104$ Jy ms is $\Gamma = -0.2 \pm 0.2$.

Ruling out aliasing. As noted in the announcement of the FRB 20180916B periodic activity discovery⁸, the best-fit cycle period could be an alias of the true period. The short CHIME/FRB exposures and their regular sidereal day sampling of $P_{\text{sid}} = 0.99727$ days lead to a degeneracy between the reported frequency $f_0 = (16.35 \text{ days})^{-1}$ and aliases of this frequency at $f_N = (Nf_{\text{sid}} \pm f_0)$, with N a positive integer and $f_{\text{sid}} = P_{\text{sid}}^{-1}$. Some periodicity models, mainly those involving ultra-long period or precessing magnetars²⁸, fit better with the shorter periods involved when $N > 0$.

To maximize the chance of detection, follow-up instruments observed FRB 20180916B predominantly around its predicted activity peak^{3,20,29,53}. The implied lack of coverage outside this purported peak could bias the derived activity cycle. Although detections of FRB 20180916B using multiple instruments and cadences have put strong constraints on allowed N values, aliasing has not been robustly ruled out until now.

To break this degeneracy, we scheduled observations covering all phases, during the first five activity cycles. Exposures lasted 3–9 h. We next generated periodograms using frbp²⁰. We employed a Pearson’s χ^2 test (PR3)⁸, an activity width minimization algorithm (R20)²¹, and a quadratic-mutual-information-based (QMI) periodicity search technique (P4J)⁵⁴. We built periodograms using bursts from Apertif only; CHIME/FRB only; CHIME/FRB plus Apertif; and from all public, known bursts. Only CHIME/FRB and Apertif have coverage and detections over the whole activity phase. The periodograms span periods between 0.01 days and 20 days to show all the aliased P_N periods for N between 0 and 37 (Extended Data Fig. 9).

The CHIME/FRB periodograms (Extended Data Fig. 9c, g, k) show numerous peaks below eight days, at the predicted aliasing values (grey vertical lines), as expected for a transit instrument. By contrast, the Apertif periodograms (Extended Data Fig. 9b, f, j) show no prominent periods below eight days beyond the broad 1-day peak in the R20 periodogram caused by the daily cadence. By next combining CHIME/FRB and Apertif bursts, the different observing cadence and exposure diminish the amplitude of most aliased peaks (Extended Data Fig. 9d, h, l). We particularly focus on the activity width minimizing plot (R20, Extended Data Fig. 9h). The low values of the maximum continuous fraction indicate that bursts are detected across the whole activity phase for all periods below eight days, allowing us to rule out any potential aliased period. This is further confirmed when adding the bursts from FRB 20180916B that were detected by other instruments, in Extended Data Fig. 9e. We conclude there is no aliasing.

To best estimate the period, we also generated wider, 1.57–60-day periodograms. The best-fit values of the peaks at about 16 days are listed in Extended Data Fig. 9a–l. Error bars represent the full-width at half maximum (FWHM) of the peaks. The fewer cycles covered by Apertif observations translate as an uncertainty larger than one day in the period estimation with the PR3 and R20 techniques, in contrast with the period estimation using CHIME/FRB bursts only. The combination of CHIME/FRB and Apertif bursts gives a period of 16.29 days with the PR3 test. The activity width minimization technique (R20) gives the most consistent period estimates when applied to different instrument combinations. We find the best-fit period is 16.29 days, where reference MJD 58369.9 centres the peak activity day at phase 0.5. This is the only period for which no bursts lie outside a 6.1-day activity window.

Activity windows. By using the above-mentioned best period and reference MJD to compute the burst arrival phases, we have generated

a histogram of detections versus phase shown in Extended Data Fig. 4a. The cycle coverage by different instruments can be visualized in Extended Data Fig. 4b, where it is manifest that CHIME/FRB and Apertif are the only instruments covering the whole activity cycle that have detected bursts. We have used data from all FRB 20180916B observations published thus far^{3,8,14,20,30,53,55,56}.

Several theoretical models have suggested the activity window may be chromatic^{22,23,28}. In absorptive wind models, for example, one expects a larger duty cycle at high frequencies due to heightened opacity at long wavelengths. There was also an observational hint that higher frequencies may arrive earlier, based on four EVN detections at 1.7 GHz (ref.¹⁴). By taking into account the bursts detected by Apertif, CHIME/FRB and LOFAR at 1.4 GHz, 600 MHz and 150 MHz, respectively, we can obtain an estimate of the probability of the bursts being drawn from the same distribution at different frequencies.

To do so, we attempted to estimate the detection rate as a function of activity phase for the three different frequency bands. We estimate these activity windows by computing the probability density function (PDF) of detection rate for Apertif, CHIME/FRB and LOFAR using a weighted kernel density estimator (KDE). The KDE is a non-parametric smoothing technique in which a kernel is built at each data point from a sample and their contributions are summed to estimate an unknown PDF. With $\{X_i; i=1, 2, \dots, n\}$ the observed data, a sample of n observations drawn from a distribution $f(x)$ with an unknown density, we define its weighted KDE in the general case as

$$\hat{f}(x) = \frac{1}{h} \sum_{i=1}^n p_i K\left(\frac{X_i - x}{h}\right), \quad (1)$$

with K the kernel function, $h > 0$ the bandwidth, and $\{p_i; i=1, \dots, n\}$ the probability weights of each data sample. In this case, the input data \mathbf{X} are the activity phases of each of the n detections and the weights \mathbf{p} are the inverse of the reciprocal observing time at that phase, and hence $\hat{f}(x)$ is the equivalent of a detection rate. We used a Gaussian function as kernel K and applied Scott’s rule for bandwidth selection⁵⁷, thus having

$$h = n_{\text{eff}}^{-1/(d+4)} = n_{\text{eff}}^{-1/5}, \quad (2)$$

with $d = 1$ the number of dimensions and n_{eff} the effective number of data points, that differs from n when applying a weighted KDE,

$$n_{\text{eff}} = \frac{\left(\sum_{i=1}^n p_i\right)^2}{\sum_{i=1}^n p_i^2}. \quad (3)$$

We applied the KDE separately to the Apertif, CHIME/FRB and LOFAR burst data sets. On the basis of the KDE estimation shown in Fig. 4, we find that higher frequencies appear to arrive earlier in phase, that is, the activity peaks at a lower phase with larger frequencies. Additionally, the width of the activity window appears to be larger with CHIME/FRB. The KDE is useful for estimating probability distributions with a small number of samples, but it is non-parametric and does not easily allow us to compare the activity window widths between frequencies. For this we fit a Gaussian to the detection rate of FRB 20180916B for each instrument and find a full-width at half maximum (FWHM) of 1.2 ± 0.1 days from the Apertif data at 1,370 MHz and 2.7 ± 0.2 days at 400–800 MHz using the CHIME/FRB bursts. The best-fit peak activity phase for Apertif is 0.494 ± 0.002 and 0.539 ± 0.005 for CHIME/FRB. The source activity window is therefore roughly two times wider at CHIME/FRB than at Apertif and its peak is 0.7 days later at CHIME/FRB.

The CHIME/FRB detections span multiple years, while the Apertif and LOFAR detections are all in 2020. Since an error of 0.05 days in a period of about 16 days could lead to a phase delay of about 0.15 after two years and thus to a broadening of the resulting activity window, we

Article

compared the PDF including all CHIME/FRB bursts with what would be obtained only with the bursts detected before 2020 and during 2020. We observe that the three CHIME/FRB distributions are consistent with each other, and all are both wider and later in arrival phase than the Apertif profile.

We do not attempt to fit a Gaussian to the LOFAR bursts because of the small number of detections and our limited coverage in phase. However, we note that four out of the nine detected LOFAR bursts arrive later in phase than every previously detected CHIME/FRB burst. Therefore, the activity of FRB 20180916B at 150 MHz probably peaks later than at higher frequencies and the activity window may be wider as well. This is in stark contrast with the predictions of simple absorptive wind models where the activity ought to be wider at higher frequencies.

To quantify the statistical significance of the phase-window differences visible in Fig. 4, we compared each pair of burst ensembles from Apertif, CHIME/FRB and LOFAR, using Kolmogorov–Smirnov (KS) tests. For KS test P values <0.01 we can reject the null hypothesis that the observed samples are drawn from the same distribution. This is the case for all pairs: for Apertif versus CHIME/FRB samples, $P = 1.71 \times 10^{-7}$; for Apertif versus LOFAR, $P = 8.45 \times 10^{-10}$; and for CHIME/FRB versus LOFAR, $P = 7.64 \times 10^{-5}$.

We next investigate whether the difference in observing strategies could cause these arrival differences. Although CHIME/FRB and Apertif cover the activity phase similarly, the per-cycle sampling function is different. After all, per day, the tracking Westerbork dishes can see FRB 20180916B for about 12 h, while the transit at CHIME/FRB lasts approximately 20 min. We therefore test whether selection effects influenced the inferred activity window, and if the different observing strategies led to other bias in the observed PDFs such as activity period jitter. To this end we simulated observed bursts drawn from a single Gaussian-distributed intrinsic population.

We first draw the number of bursts per cycle N from a normal distribution centred at the CHIME/FRB average rate, $R \approx 0.32 \text{ h}^{-1} \approx 125 \text{ per cycle}$, for a period $P = 16.29 \text{ days}$, with standard deviation $R/5 \approx 25 \text{ per cycle}$. We next draw burst arrival phases from a normal distribution centred at CHIME/FRB phase centre 0.52, with standard deviation 2.73 days or about 0.17 in phase. We count the bursts Apertif, CHIME/FRB and LOFAR would have detected at their respective observing sessions. We compare the resulting simulated periodograms between pairs of telescopes in the same way as we compared the actual periodograms. We perform this simulation 10^5 times (Extended Data Fig. 5).

These activity-window selection effect simulations discard Apertif and CHIME/FRB burst samples as drawn from the same distribution at a 4.1σ level. The Apertif and LOFAR burst distributions are ruled out as being the same with 3.8σ confidence. For both, the actual P values are well below 99.73% (3σ) of the simulated P values (Extended Data Fig. 5). The activity windows are indeed different and are not due to an observational bias. By itself, the observed CHIME/FRB–LOFAR P value is at 2.7σ of the simulated P values. The LOFAR detections are fewest, and the activity windows at CHIME/FRB and LOFAR are closer to one another. However, we note that four of the LOFAR detections in a single activity cycle arrive later in phase than any previously detected CHIME/FRB burst.

Thus, taking all observational biases into account, a frequency dependence of the activity window must exist to reproduce the observed burst distribution. It peaks earlier at higher frequencies. Additional LOFAR bursts have been reported¹¹ that confirm the later activity phase at lower frequencies. The burst window is also more than $2\times$ wider at low frequencies. This is opposite to the predictions from models in which free–free absorption in the stellar wind of a binary companion directly produces the periodicity, where lower frequency emission windows should be narrower^{22,23}, not wider. Our results thus disfavour the cause of the periodicity being free–free absorption in a binary system.

Bursts following radius-to-frequency mapping in an emitting magnetosphere swept back by binary orbital motion¹¹ could exhibit the

observed frequency-dependent phase delays. Such a model does not, however, produce the required reversal of the absorptive width versus frequency relationship. The absorption characteristics of the material outside the trailing funnel are unchanged. The radius-to-frequency mapping required to reproduce the delay relationship depends on highly localized emitting regions for each observed phase angle⁵⁸. It is as yet unclear whether such models can easily produce the substantial intrinsic widening observed for the emitting regions at later phase.

Polarization. Monitoring the polarization position angle (PA) of FRB 20180916B over time and across cycles with Apertif is made easier by the fact that Westerbork is a steerable equatorial mount telescope. This stability of the system’s response allows us to investigate the polarization properties of FRB 20180916B within each pulse, within an activity cycle, and even between multiple periods.

The source is always in the same central beam and the on-sky feed orientation does not vary with parallactic angle. This eases the study of the intrinsic polarization PA. For lower-frequency surveys or higher-rotation-measure (RM) sources, such study is hampered by the covariance between RM and PA, where

$$\Delta PA = 2\Delta RM \lambda^2 \approx 5.5^\circ \left(\frac{\Delta RM}{1 \text{ rad m}^{-2}} \right) \left(\frac{v}{1,370 \text{ MHz}} \right)^{-2}.$$

We calibrate the Apertif polarization response by observing 3C286 and 3C147. The former is roughly 12% linearly polarized with a stable PA; the latter is known to be unpolarized, which allows us to solve for leakage from I into Q, U and V. For the analysis, we dedisperse the bursts to $348.75 \text{ pc cm}^{-3}$. We use $RM = -115 \text{ rad m}^{-2}$, a value³ corroborated by Q/U fitting using RM-Tools⁵⁹ and our own code. Compared to CHIME, our smaller $\Delta \lambda^2$ range limits our ability to identify RM variations in activity phase and across cycles. For our purpose of monitoring PA over time, we feel confident using this previously-determined RM value, especially since the Galactic Faraday foreground of $-115 \pm 12 \text{ rad m}^{-2}$ probably dominates the total RM of FRB 20180916B^{56,60}.

We find the PA of FRB 20180916B to be flat within each burst, with $\Delta PA < 20^\circ$, in agreement with other polarization studies of the source^{3,7,61}. This is in contrast to most pulsars whose PAs swing across the pulse, in many cases with the S-shaped functional form predicted by the rotating vector model. In the classic picture, PA varies with the arctangent of pulse longitude and the amount of swing is proportional to the emission height but inversely proportional to the star’s rotation period⁶². However, the flat PAs of FRB 20180916B are similar to those of other FRBs, notably FRB 20121102A whose intra-burst polarization exhibits less than 11° of rotation². They are also similar to radio magnetars. FRB 181112 was the first source to show considerable variation in the polarization state within a burst and between sub-components of an FRB with temporal structure⁶³.

While the flat PAs within each FRB 20180916B burst are in line with previous measurements, we have found that its PA is also stable on average within an activity cycle and even between periods, with $\Delta PA < 50^\circ$. In models that invoke precession as the origin of periodicity and magnetospheric emission as the origin of the FRBs, one generically expects a PA change as a function of activity phase. However, the amount of PA swing depends on the geometry of the system as well as the fraction of a precession period that is observable²⁵, so we cannot rule out precession with our polarization measurements. In relativistic shock models, the synchrotron maser mechanism provides a natural path for flat PAs within a burst, but it is not clear how or whether the polarization state could be nearly constant within a cycle and over multiple months^{27,64}. Given that the duty cycle of FRB 20180916B appears to be just about 10% in the Apertif band, it will be useful to observe the PAs of FRB 20180916B at lower frequencies with a steerable telescope that can cover a full periodic cycle.

Dispersion. The Apertif real-time FRB detection pipeline AMBER reports the DM that maximizes the S/N of a burst ($DM_{S/N}$). Any

frequency-swept structure intrinsic to the pulse, as seen in a number of repeating FRBs, will be absorbed in this value. The discovery of multiple subcomponents showing a downward drift in frequency, in bursts from the first repeating FRB (FRB 20121102A)—and later in other repeaters—motivated the development of methods that maximize DM upon structure (DM_{struct}) rather than S/N (refs. ^{2,15}). As $DM_{S/N}$ assumes that the signal can be completely described by a v^{-2} power law, DM_{struct} is more likely to represent the actual dispersive effect³⁴. If a burst shows a single component, the computed DM_{struct} is equivalent to $DM_{S/N}$. Hence, we report DM_{struct} for all Apertif bursts, which was determined using a modified version of DM_PHASE (https://www.github.com/DanieleM-ichilli/DM_phase). We define the best Apertif DM by computing the median DM_{struct} of bursts that were detected with $S/N > 20$. We obtain $DM_{\text{Apertif}} = 348.75 \pm 0.12 \text{ pc cm}^{-3}$, where the errors represent the median absolute deviation. DM_{Apertif} is consistent with values previously reported in the literature, and we use this value to create the dynamic spectra of the bursts shown in Extended Data Figs. 2, 3.

There is no evidence for a variation of DM with phase (Extended Data Fig. 6a). Within the error, the bursts are consistent with a constant $DM = 348.75 \text{ pc cm}^{-3}$. From a visual inspection of the dedispersed pulse profiles, we find that the DM of outlier bursts A08, A19, A24 and A31 could be explained by the presence of unresolved sub-bursts.

The LOFAR bursts lack detectable time–frequency structure, but require separating the frequency-dependent scattering tails from the DM fit. After initial S/N-maximization DM fitting using pdmp⁶⁵, we hence divided every profile into sub-bands, and fitted these with a scattered Gaussian each. The resulting Gaussian centres were time aligned using an additional $\tau_{\text{DM}} \propto v^{-2}$ correction. For the final LOFAR DM, obtained by averaging over all bursts with $S/N > 20$ (Extended Data Table 1), we find $DM_{\text{LOFAR}} = 349.00 \pm 0.02 \text{ pc cm}^{-3}$, with the error reporting the standard deviation.

Sub-pulse drift rate. Several FRBs exhibit downward drifting sub-pulses, in which later sub-bursts in a pulse train arrive at ever lower frequencies. Thus far, there is currently no example of upward drift within a burst. In the first known repeater, FRB 20121102A, the sub-pulses drift downward faster at higher observing frequencies^{15,19,66}. Several of our FRB 20180916B detections at Apertif show downward drifting sub-pulses, enabling us to make the first measurement of the drift rate \dot{v} of FRB 20180916B above 1 GHz (Extended Data Fig. 8).

As no scattering tails were seen above 350 MHz (refs. ^{3,7,14}), we represented each sub-burst as Gaussian in time. After dedispersing each burst to its DM_{struct} , we applied least-squares fitting to two, three, four, five or twelve sub-burst Gaussians. Each sub-pulse time range is defined by where the Gaussian peak exceeds the baseline noise by $>2\sigma$. We next fitted each component as a Gaussian in frequency. A linear fit to the resulting time–frequency sub-pulse centroids finally produced the burst drift rate. Extended Data Figure 8 illustrates different burst morphologies and number of components.

We obtain an average sub-pulse drift rate of $-39 \pm 7 \text{ MHz ms}^{-1}$ at 1,370 MHz, where we quote the standard error on the mean. The standard deviation of the sample is 31 MHz ms^{-1} . This drift rate is nine times larger than, for example, the one reported³ at 400 MHz of about -4.2 MHz ms^{-1} . The downward drift amplifies towards higher frequencies. We quantify the drift rate evolution by fitting a power law $\dot{v} = k_p v^\gamma$, with k_p a constant and γ the power-law index, and a linear function $\dot{v} = k_l v$ with k_l a constant. Neither model allows drift rates to turn from negative to positive at a frequency $v > 0$, which we do not deem physically possible. A least squares minimization fit to the power law gives $\gamma = 0.7 \pm 0.4$ and $k_p = -0.2 \pm 0.6$, close to linear. The linear function itself is best fitted as $k_l = -(2.9 \pm 0.4) \times 10^{-2}$. By scaling the fitted functions to the frequency of the LOFAR High Band Antenna, we would expect the drift rate to be around -6 MHz ms^{-1} at 150 MHz. The apparent lack of multiple components in the LOFAR bursts does not allow us to confirm this. Overall, as in FRB 20121102A¹⁹, the drift rate evolution appears

linear. As these two FRBs reside in considerably different environments, the behaviour may be common across FRBs. The frequency-dependence and consistent sign of the drifting phenomenon will probably offer clues to the FRB emission mechanism^{27,67,68}.

Scattering. Most of the LOFAR bursts (Fig. 2) exhibit an exponential tail, indicating the pulse-broadening due to scattering in the intervening medium. To quantify the scatter broadening timescale (τ_{sc}), we divided the dedispersed spectrograms of a few high-S/N bursts into four or eight sub-bands. The burst profiles obtained from the individual sub-bands were modelled as a single Gaussian component convolved with a one-sided exponential function^{69,70}. The τ_{sc} thus obtained are presented in Extended Data Table 1.

To obtain a more precise estimate of scatter-broadening timescale, we first divided the bandwidth of the stacked LOFAR bursts dedispersed to their $DM_{\text{LOFAR}} = 349.0 \text{ pc cm}^{-3}$ into eight frequency bands, for which we obtained separate pulse profiles and fitted each to a scattering tail as above. The results are shown in Extended Data Fig. 6. We obtain the scattering timescale of $45.7 \pm 9.5 \text{ ms}$ at 150 MHz, which is consistent with the measurements using individual bursts. We also characterize the scatter-broadening variation with frequency as $\tau_{\text{sc}} \propto v^{-\alpha}$ and obtain the frequency scaling index $\alpha = -4.2^{+1.1}_{-1.0}$. This scatter-broadening is consistent with the upper limit of 50 ms at 150 MHz that was derived from GBT detections at 350 MHz (ref. ³). By scaling the scatter broadening of LOFAR bursts to Apertif frequencies, we expect $\tau_{\text{sc}} \approx 6.6 \mu\text{s}$ at 1,370 MHz, which is an order of magnitude smaller than Apertif's temporal resolution.

The observed scattering time is within a factor of two of the predicted Galactic scattering¹⁶. Thus, we attribute this pulse broadening to scattering in the Milky Way interstellar medium (ISM) and not to plasma in the host galaxy. The fact that the ISM scattering is stronger in the Milky Way than in the host galaxy is not surprising, given FRB 20180916B is at a low Galactic latitude, whereas its host is a nearly face-on spiral galaxy¹⁴.

Rates. Before our LOFAR detections, there existed only upper limits on the FRB sky rate below 200 MHz. Blind searches for fast transients at these low frequencies are difficult owing to the deleterious smearing effects of intra-channel dispersion and scattering, which scale as v^{-3} and v^{-4} , respectively. This is amplified by the large sky brightness temperatures at long wavelengths, due to the red spectrum of Galactic synchrotron emission; pulsars are detectable at low frequencies because of their steeply rising negative spectra, but the spectral index of the FRB event rate is not known. We first consider the repetition rate of FRB 20180916B from our LOFAR and Apertif detections to determine its activity as function of frequency. We then convert that into a lower-limit on the all-sky FRB rate at 150 MHz and combine it with previous upper limits at those frequencies to derive the first bounded constraints on FRB rates below 200 MHz.

We detected nine bursts in 48 h of LOFAR observing, giving a rate of $0.19 \pm 0.06 \text{ h}^{-1}$. Since we only targeted LOFAR during simultaneous Apertif observations during the presumed activity window whose duty cycle is about 0.25, we divide this rate by four to get its repetition rate averaged over time. Assuming a fluence threshold of 50 Jy ms and noting that the duration of all bursts from this source at 150 MHz is set by scattering and does not vary, we find $R_{150}(\geq 50 \text{ Jy ms}) \approx (4.6 \pm 1.6) \times 10^{-2} \text{ h}^{-1}$. At 1,370 MHz, Apertif detected 54 pulses in 388 h of observing. Our coverage of FRB 20180916B was deliberately more uniform in activity phase, so only about 149 h took place during the active days. The phase range in which Apertif detected bursts gives a duty cycle of 0.22. This results in $R_{1,370}(\geq 1 \text{ Jy ms}) \approx (8.0 \pm 1.1) \times 10^{-2} \text{ h}^{-1}$. While the absolute detection rates by Apertif and LOFAR are similar, we note that the fluence threshold was much lower for Apertif than LOFAR. Scaling by the approximate fluence distribution of FRB 20180916B, $N(\geq \mathcal{F}) \propto \mathcal{F}^{-1.5}$ (ref. ⁸), we find $R_{1,370}(\geq 50 \text{ Jy ms}) \approx 2.3 \times 10^{-4} \text{ h}^{-1}$. We come to the

Article

remarkable conclusion that the FRB is two orders of magnitude more active at 150 MHz than at 1,370 MHz at the relevant fluences.

The all-sky FRB event rate is a difficult quantity to determine for myriad reasons⁷¹. Beam effects result in a pointing-dependent sensitivity threshold^{72,73}, and each survey has back-end-dependent incompleteness, hindering FRB detection for ranges of flux density and fluence⁷⁴ as well as pulse duration and DM⁷⁵. Nonetheless, meaningful constraints can be made if one is explicit about the region of parameter space to which the rate applies.

As the LOFAR bursts are the sole unambiguous FRB detections below 200 MHz, we and other teams¹¹ can now provide the first bounded limits on the all-sky event rate at low frequencies. A lower limit on the FRB rate at 150 MHz can be obtained by assuming FRB 20180916B is the only source in the sky emitting at these wavelengths. This lower bound can be combined with previous upper bounds from non-detections by blind searches at LOFAR and MWA^{12,13,76–79}. The repetition rate of FRB 20180916B implies that there are at least 0.6 d^{-1} over the whole sky above 50 Jy ms at 110–190 MHz at 95% confidence. Assuming a Euclidean scaling in the brightness distribution that continues down to lower fluences, this is equivalent to more than 90 d^{-1} over the whole sky above 5 Jy ms. An earlier blind LOFAR search¹³ placed an upper limit of 29 d^{-1} over the whole sky above 62 Jy pulses with 5 ms duration. Combining these two limits, we obtain a 90% confidence region of $3\text{--}450 \text{ d}^{-1}$ over the whole sky above 50 Jy ms.

The lower-limit value may be conservative, as FRB 20180916B is in the Galactic plane at a latitude of just 3.7° , which is why its scattering time is 50 ms at 150 MHz. If the burst width were 5 ms before entering the Milky Way, then a factor of about 3 was lost in S/N due to the low Galactic latitude of FRB 20180916B. Therefore, a similar FRB at a more typical offset from the plane would, in this example, be about 3° times more active, in which γ is the cumulative energy distribution power-law index, because the Galactic scattering timescale would only be a few milliseconds.

Data availability

Raw data were generated by the Apertif system on the Westerbork Synthesis Radio Telescope and by the International LOFAR Telescope. The Apertif data that support the findings of this study are available through the ALERT archive, <http://www.alert.eu/FRB20180916B>. The LOFAR data are available through the LOFAR Long Term Archive, <https://lta.lofar.eu/>, by searching for ‘Observations’ at J2000 coordinates RA = 01:57:43.2000, Dec. = +65:42:01.020, or by selecting COM_ALERT in ‘Other projects’ and downloading data which includes R3 in the ‘Observation description’.

Code availability

The custom code used to generate these results is publicly available at <https://doi.org/10.5281/zenodo.4559593> (ref. ⁸⁰).

31. Oosterloo, T., Verheijen, M. & van Cappellen, W. The latest on Apertif. In Proc. ISKAF2010 Science Meeting 043 (Proceedings of Science, Vol. 112, 2010).
32. Adams, E. A. K. & van Leeuwen, J. Radio surveys now both deep and wide. *Nature Astron.* **3**, 188 (2019).
33. Connor, L. et al. A bright, high rotation-measure FRB that skewers the M33 halo. *Mon. Not. R. Astron. Soc.* **499**, 4716–4724 (2020).
34. Oostrum, L. C. et al. Repeating fast radio bursts with WSRT/Apertif. *Astron. Astrophys.* **635**, A61 (2020).
35. van Leeuwen, J. ARTS – the Apertif Radio Transient System. In Proc. The Third Hot-wiring the Transient Universe Workshop <https://www.slac.stanford.edu/econf/C131113/> proceedings.html (eds Wozniak, P. R., Graham, M. J., Mahabal, A. A. & Seaman, R.) 79 (LANL, 2014).
36. Oostrum, L. C. Fast Radio Bursts with Apertif. PhD thesis, Univ. Amsterdam (2020).
37. Sclocco, A., van Leeuwen, J., Bal, H. E. & van Nieuwpoort, R. V. Real-time dedispersion for fast radio transient surveys, using auto tuning on many-core accelerators. *Astronomy and Computing* **14**, 1–7 (2016).
38. Sclocco, A., Heldens, S. & van Werkhoven, B. AMBER: a real-time pipeline for the detection of single pulse astronomical transients. *SoftwareX* **12**, 100549 (2020).
39. Sclocco, A., Vohl, D. & van Nieuwpoort, R. V. Real-time rfi mitigation for the apertif radio transient system. In Proc. 2019 RFI Workshop — Coexisting with Radio Frequency Interference (RFI) 1–8 (IEEE, 2019).
40. Oostrum, L. C. loostrum/darc: version 2.1. <https://doi.org/10.5281/zenodo.3784870> (2020).
41. Connor, L. & van Leeuwen, J. Applying deep learning to fast radio burst classification. *Astron. J.* **156**, 256 (2018).
42. Yao, J. M., Manchester, R. N. & Wang, N. A new electron density model for estimation of pulsar and FRB distances. *Astrophys. J.* **835**, 29 (2017).
43. Ransom, S. M. *New Search Techniques For Binary Pulsars*. Ph.D. thesis, Harvard Univ. (2001).
44. van Haarlem, M. P. et al. LOFAR: The Low-Frequency ARray. *Astron. Astrophys.* **556**, A2 (2013).
45. Maan, Y., van Leeuwen, J. & Vohl, D. Fourier domain excision of periodic radio frequency interference. *Astron. Astrophys.* **650**, A80 (2021).
46. Perley, R. A. & Butler, B. J. An accurate flux density scale from 50 MHz to 50 GHz. *Astrophys. J. Suppl. Ser.* **230**, 7 (2017).
47. Cordes, J. M. & McLaughlin, M. A. Searches for fast radio transients. *Astrophys. J.* **596**, 1142–1154 (2003).
48. Maan, Y. & Aswathappa, H. A. Deep searches for decametre-wavelength pulsed emission from radio-quiet gamma-ray pulsars. *Mon. Not. R. Astron. Soc.* **445**, 3221–3228 (2014).
49. Houben, L. J. M. et al. Constraints on the low frequency spectrum of FRB 121102. *Astron. Astrophys.* **623**, A42 (2019).
50. Sanidas, S. et al. The LOFAR Tied-Array All-Sky Survey (LOTAAS): survey overview and initial pulsar discoveries. *Astron. Astrophys.* **626**, A104 (2019).
51. Konratiev, V. I. et al. A LOFAR census of millisecond pulsars. *Astron. Astrophys.* **585**, A128 (2016).
52. Bilous, A. V. et al. A LOFAR census of non-recycled pulsars: average profiles, dispersion measures, flux densities, and spectra. *Astron. Astrophys.* **591**, A134 (2016).
53. Pilia, M. et al. The lowest frequency fast radio bursts: Sardinia Radio Telescope detection of the periodic FRB 180916 at 328 MHz. *Astrophys. J.* **896**, L40 (2020).
54. Huijse, P. et al. Robust period estimation using mutual information for multiband light curves in the synoptic survey era. *Astrophys. J. Suppl. Ser.* **236**, 12 (2018).
55. Scholz, P. et al. Simultaneous X-ray and radio observations of the repeating fast radio burst FRB 180916.J0158+65. *Astrophys. J.* **901**, 165 (2020).
56. Pearlman, A. B. et al. Multiwavelength radio observations of two repeating fast radio burst sources: FRB 121102 and FRB 180916.J0158+65. *Astrophys. J.* **905**, L27 (2020).
57. Scott, D. W. *Multivariate Density Estimation: Theory, Practice, and Visualization* (Wiley & Sons, 2015).
58. Lyutikov, M. Radius-to-frequency mapping and FRB frequency drifts. *Astrophys. J.* **889**, 135 (2020).
59. Purcell, C. R., Van Eck, C. L., West, J., Sun, X. H. & Gaensler, B. M. RM-Tools: rotation measure (RM) synthesis and Stokes QU-fitting. (Astrophysics Source Code Library, ascl:2005.003, 2020).
60. Ordog, A., Booth, R. A., Van Eck, C. L., Brown, J.-A. C. & Landecker, T. L. Faraday rotation of extended emission as a probe of the large-scale galactic magnetic field. *Galaxies* **7**, 43 (2019).
61. Nimmo, K. et al. Highly polarized microstructure from the repeating FRB 20180916B. *Nature Astron.* **5**, 594–603 (2021).
62. Blaskiewicz, M., Cordes, J. M. & Wasserman, I. A relativistic model of pulsar polarization. *Astrophys. J.* **370**, 643 (1991).
63. Cho, H. et al. Spectropolarimetric analysis of FRB 181112 at microsecond resolution: implications for fast radio burst emission mechanism. *Astrophys. J. Lett.* **891**, L38 (2021).
64. Beloborodov, A. M. A flaring magnetar in FRB 121102? *Astrophys. J.* **843**, L26 (2017).
65. Hotan, A. W., van Straten, W. & Manchester, R. N. Psrchive and Psrfits: an open approach to radio pulsar data storage and analysis. *Publ. Astron. Soc. Aust.* **21**, 302–309 (2004).
66. Caleb, M. et al. Simultaneous multi-telescope observations of FRB 121102. *Mon. Not. R. Astron. Soc.* **496**, 4565–4573 (2020).
67. Wang, W., Zhang, B., Chen, X. & Xu, R. On the time-frequency downward drifting of repeating fast radio bursts. *Astrophys. J.* **876**, L15 (2019).
68. Rajabi, F., Chamma, M. A., Wyenberg, C. M., Mathews, A. & Houde, M. A simple relationship for the spectro-temporal structure of bursts from FRB 121102. *Mon. Not. R. Astron. Soc.* **498**, 4936–4942 (2020).
69. Krishnakumar, M. A., Joshi, B. C. & Manoharan, P. K. Multi-frequency scatter broadening evolution of pulsars. I. *Astrophys. J.* **846**, 104 (2017).
70. Maan, Y., Joshi, B. C., Surnis, M. P., Bagchi, M. & Manoharan, P. K. Distinct properties of the radio burst emission from the magnetar XTE J1810–197. *Astrophys. J.* **882**, L9 (2019).
71. Rane, A. et al. A search for rotating radio transients and fast radio bursts in the Parkes high-latitude pulsar survey. *Mon. Not. R. Astron. Soc.* **455**, 2207–2215 (2016).
72. Lawrence, E., Wiel, S. V., Law, C. J., Spolaor, S. B. & Bower, G. C. The non-homogeneous Poisson process for fast radio burst rates. *Astron. J.* **154**, 117 (2017).
73. Vedantham, H. K., Ravi, V., Hallinan, G. & Shannon, R. The fluence and distance distributions of fast radio bursts. *Astrophys. J.* **830**, 75 (2016).
74. Keane, E. F. & Petroff, E. Fast radio bursts: search sensitivities and completeness. *Mon. Not. R. Astron. Soc.* **447**, 2852–2856 (2015).
75. Connor, L. Interpreting the distributions of FRB observables. *Mon. Not. R. Astron. Soc.* **487**, 5753–5763 (2019).
76. ter Veen, S. et al. The FRATS project: real-time searches for fast radio bursts and other fast transients with LOFAR at 135 MHz. *Astron. Astrophys.* **621**, A57 (2019).
77. Tingay, S. J. et al. A search for fast radio bursts at low frequencies with Murchison Widefield Array high time resolution imaging. *Astron. J.* **150**, 199 (2015).
78. Rowlinson, A. et al. Limits on fast radio bursts and other transient sources at 182 MHz using the Murchison Widefield Array. *Mon. Not. R. Astron. Soc.* **458**, 3506–3522 (2016).
79. Sokolowski, M. et al. No low-frequency emission from extremely bright fast radio bursts. *Astrophys. J.* **867**, L12 (2018).
80. Pastor-Marazuela, I. Reproduction package for “Chromatic periodic activity down to 120 megahertz in a fast radio burst”. <https://doi.org/10.5281/zenodo.4559593> (2021).

Acknowledgements This research was supported by the European Research Council under the European Union's Seventh Framework Programme (FP/2007-2013)/ERC grant agreement no. 617199 ('ALERT'), and by Vici research programme 'ARGO' with project number 639.043.815, financed by the Dutch Research Council (NWO). Instrumentation development was supported by NWO (grant 614.061.613 ARTS) and the Netherlands Research School for Astronomy ('NOVA4-ARTS', 'NOVA-NW3' and 'NOVA5-NW3-10.3.5.14'). PI of aforementioned grants is J.v.L. We further acknowledge funding from an NWO Veni Fellowship to E.P., from Netherlands eScience Center (NLeSC) grant ASDL15.406 to D.V. and A.S., from National Aeronautics and Space Administration (NASA) grant number NNX17AL74G issued through the NNNH16ZDAO01IN Astrophysics Data Analysis Program (ADAP) to S.S.; by the WISE research programme, financed by NWO, to E.A.K.A.; from FP/2007-2013 ERC grant agreement no. 291531 ('HIStoryNU') to T.v.d.H.; and from VINNOVA VINNMER grant 2009-01175 to V.M.I. I.P.-M. and Y.M. thank M. A. Krishnakumar for providing a software module that was useful in estimating the scatter-broadening timescale. This work makes use of data from the Apertif system installed at the Westerbork Synthesis Radio Telescope owned by ASTRON. ASTRON, the Netherlands Institute for Radio Astronomy, is an institute of NWO. This paper is based (in part) on data obtained with the International LOFAR Telescope (ILT) under project code COM ALERT. These data are accessible through the LOFAR Long Term Archive, <https://ita.lofar.eu/>. LOFAR (Methods) is the low frequency array designed and constructed by ASTRON. It has observing, data processing and data storage facilities in several countries, that are owned by various parties (each with their own funding sources), and that are collectively operated by the ILT foundation under a joint scientific policy. The ILT resources have benefitted from the following recent major funding sources: CNRS-INSU, Observatoire de Paris and Université

d'Orléans, France; BMBF, MIWF-NRW, MPG, Germany; Science Foundation Ireland (SFI), Department of Business, Enterprise and Innovation (DBEI), Ireland; NWO, The Netherlands; The Science and Technology Facilities Council, UK; Ministry of Science and Higher Education, Poland. We acknowledge use of the CHIME/FRB Public Database, provided at <https://www.chime-frb.ca> by the CHIME/FRB Collaboration.

Author contributions I.P.-M., L.C., J.v.L., Y.M., S.t.V., A.B., L.O., E.P., S.S. and D.V. analysed and interpreted the data. I.P.-M., L.C., J.v.L., Y.M. and S.t.V. contributed to the LOFAR data acquisition, and to the conception, design and creation of LOFAR analysis software. I.P.-M., L.C. and J.v.L. conceived and drafted the work, and Y.M., S.t.V., A.B., L.O., E.P., S.S. and D.V. contributed substantial revisions. L.O., J.A., O.M.B., E.K., D.v.d.S., A.S., R.S., E.A.K.A., B.A., W.J.G.d.B., A.H.W.M.C., S.D., H.D., K.M.H., T.v.d.H., B.H., V.M.I., A.K., G.M.L., D.M.L., A.M., V.A.M., H.M., M.J.N., T.O., E.O., M.R. and S.J.W. contributed to the conception, design and creation of the Apertif hardware, software and firmware used in this work, and to the Apertif data acquisition.

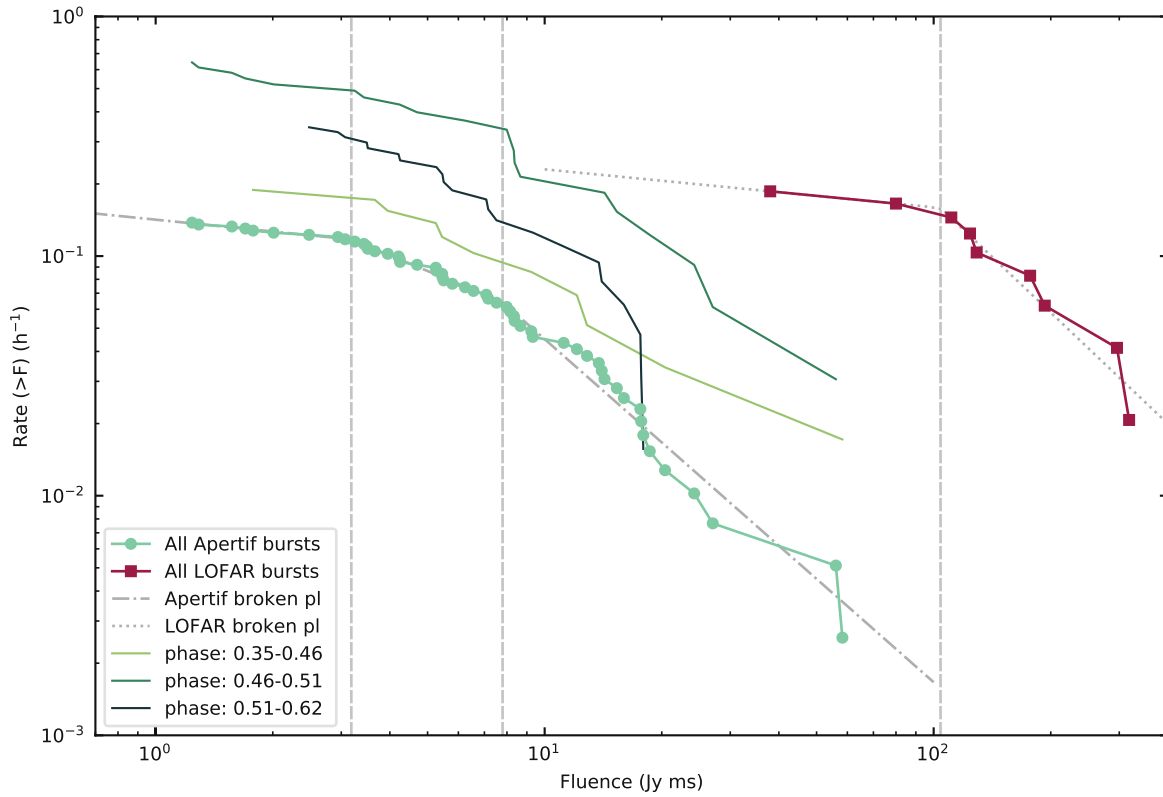
Competing interests The authors declare no competing interests.

Additional information

Correspondence and requests for materials should be addressed to J.v.L.

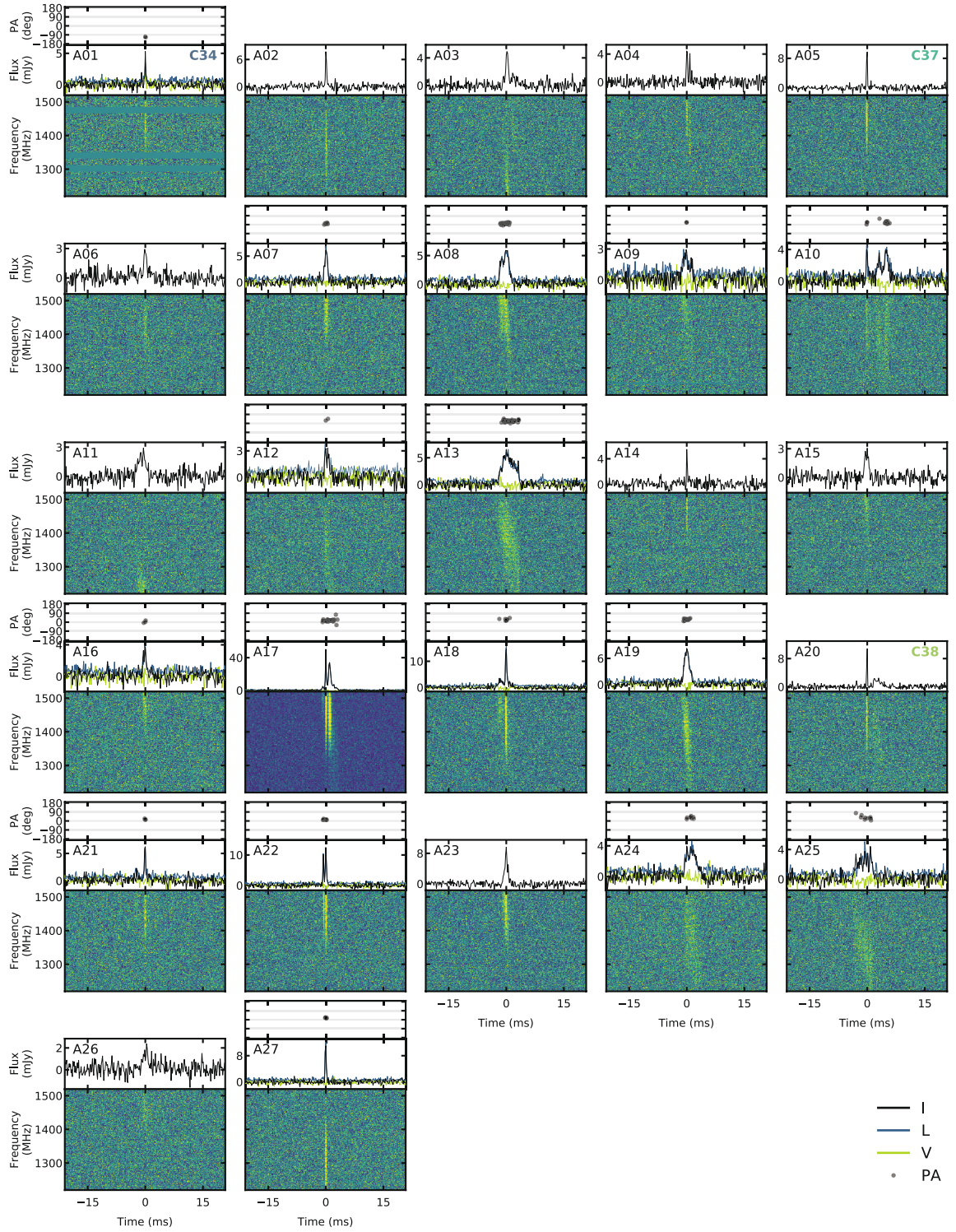
Peer review information *Nature* thanks Scott Ransom and Matthew Bailes for their contribution to the peer review of this work.

Reprints and permissions information is available at <http://www.nature.com/reprints>.


Extended Data Fig. 1 | The FRB 20180916B fluence distribution at Apertif

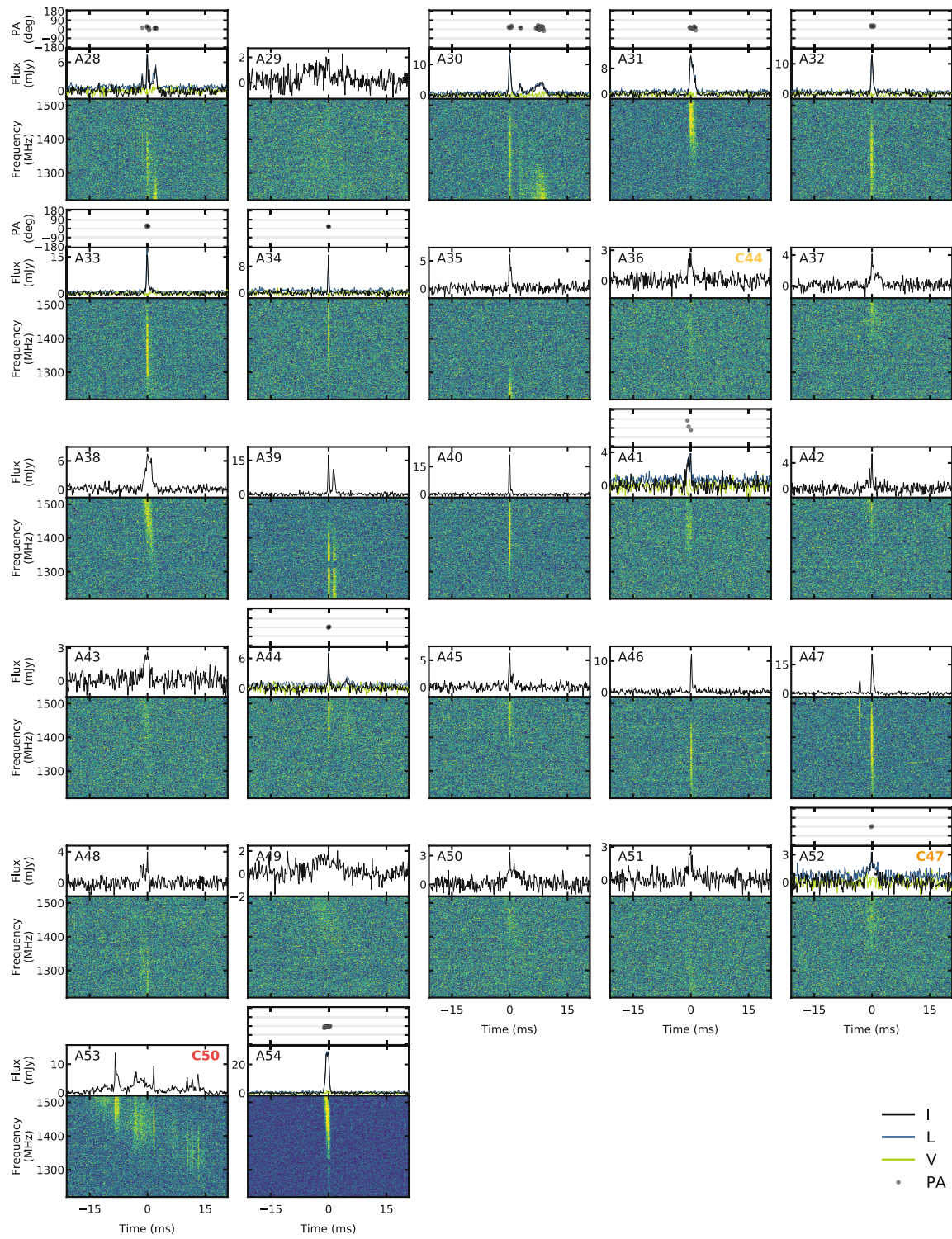
and at LOFAR. For each fluence F we plot how many brighter bursts are detected per hour, Rate ($>F$) (h^{-1}). The light green data points show the cumulative distribution function (CDF) of all Apertif bursts, with dash-dotted, dotted and dashed lines giving the power-law fit respectively to bursts with fluences lower than 3.2 Jy ms, between 3.2 Jy ms and 7.8 Jy ms, and above

7.8 Jy ms. The coloured solid lines correspond to different phase ranges within the active window, with no discernible difference between them other than the rate scaling. The LOFAR fluence distribution is shown in crimson. The fit to a broken power law ('broken pl') with a fluence turnover at 104 Jy ms is shown as a grey dotted line. For the same fluence, FRB 20180916B is more active at 150 MHz than 1,370 MHz, even at the peak activity phases observed by Apertif.

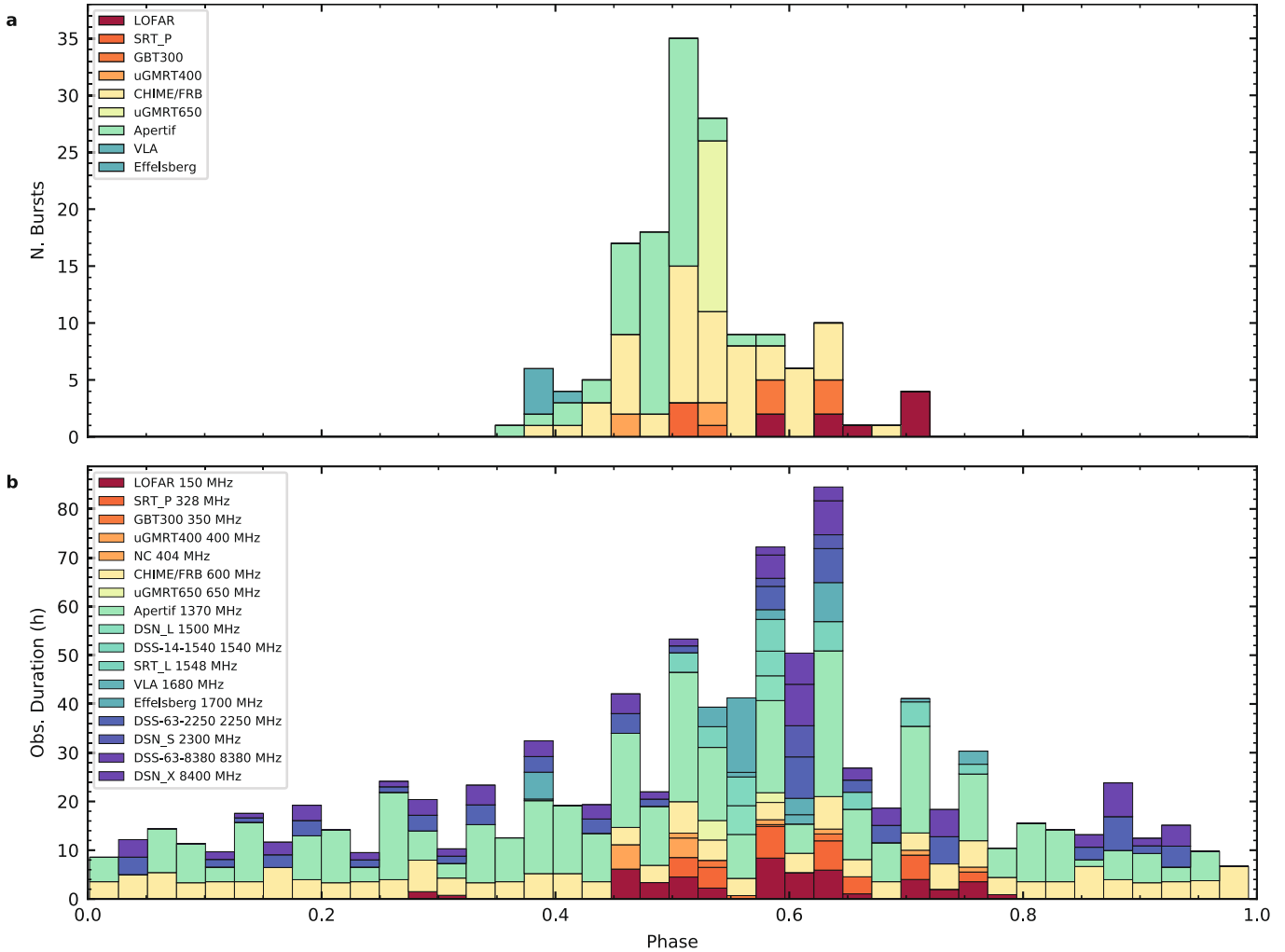


Extended Data Fig. 2 | Dynamic spectra of Apertif bursts A01–A27. We display PA (top panel), Stokes parameters I, L and V (central panel) and dynamic spectra (bottom panel), for bursts with full Stokes data (for example, panel A01 at top left). Bursts with only intensity data, such as A02, are limited to the total

intensity profile. Burst identifiers are given in the top-left corners, and activity cycle number in the top-right corners. Data have been dedispersed to $DM = 348.75 \text{ pc cm}^{-3}$, and downsampled 2 \times in time and 8 \times in frequency.



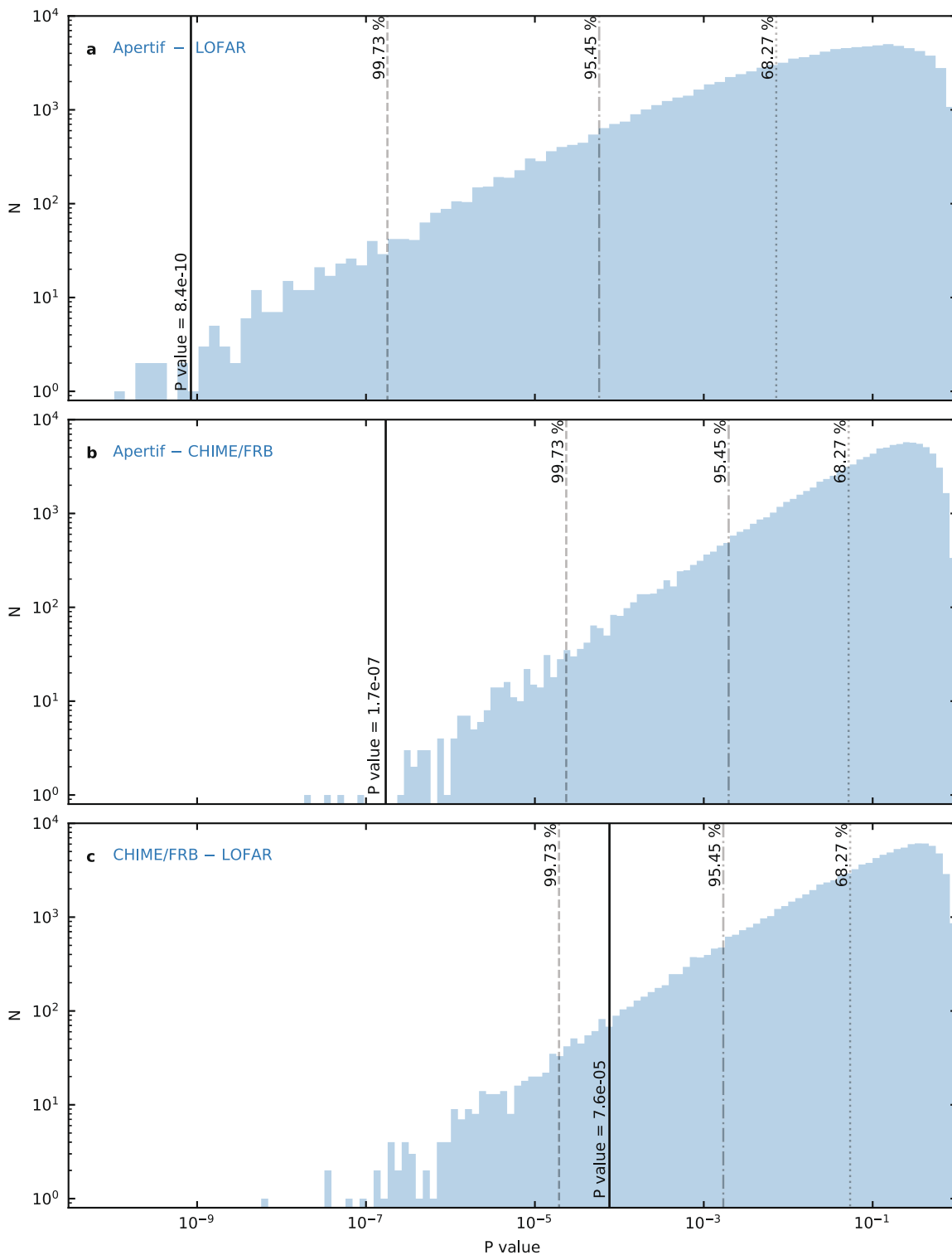
Extended Data Fig. 3 | Dynamic spectra of Apertif bursts A28–A54. As in Extended Data Fig. 2.



Extended Data Fig. 4 | Observations and detections as a function of phase.

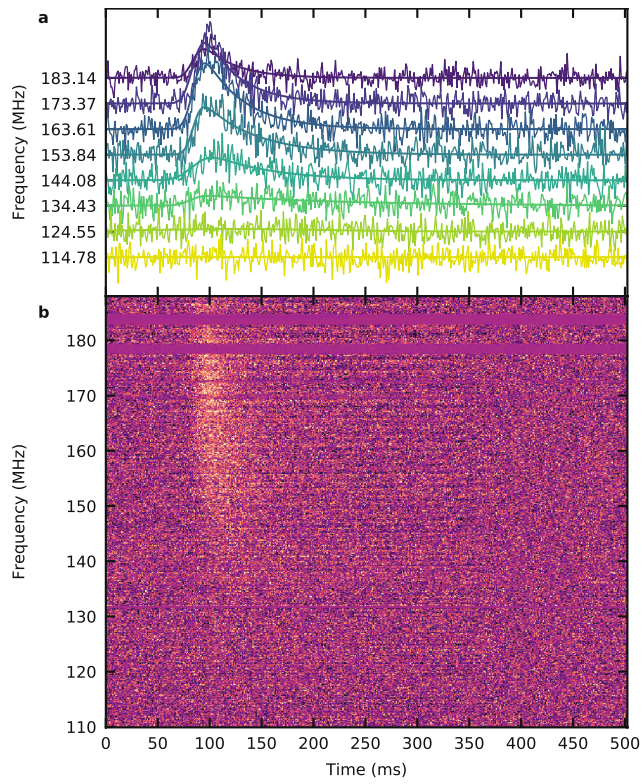
a, b, Shown are histograms of burst detections ('N. Bursts'; **a**) and of observation duration ('Obs. Duration'; **b**), both as a function of phase for the best period fitted to Apertif and CHIME/FRB data (16.29 days). In both panels,

instruments are colour-coded by central frequency, with blue for high frequencies and red for low frequencies. This figure was generated using an adaptation of the `frbpap` package²⁰.

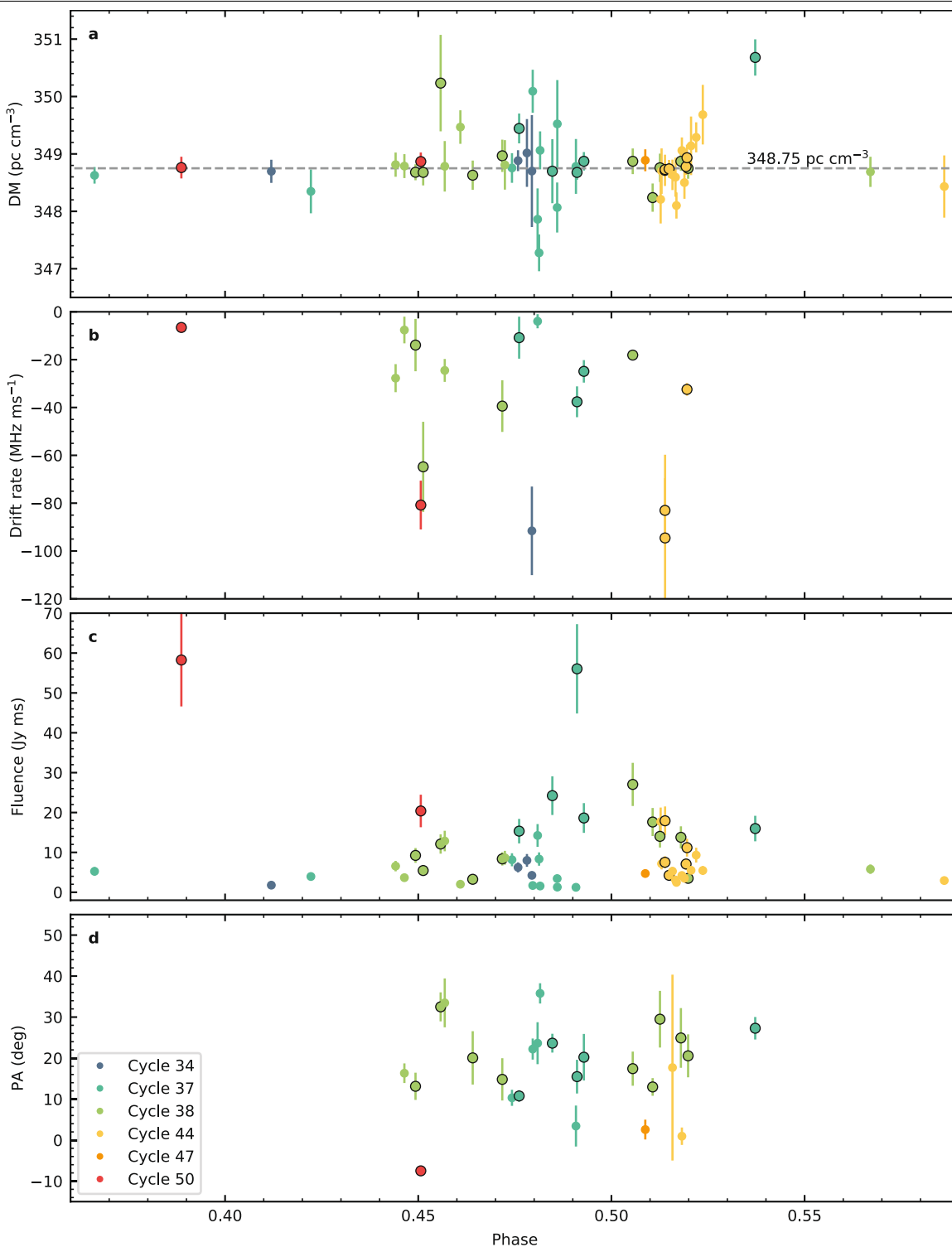


Extended Data Fig. 5 | Comparison of simulated and observed activity window Pvalues. **a–c**, Each panel compares the P value obtained through the Kolmogorov–Smirnov statistic on two instrument burst samples. The vertical black lines give the observed P value, whereas the histograms correspond to 10^5 simulations of the P value that would be obtained if both instrument burst samples were drawn from the same distribution. N is the number of resulting

simulations per P value. Shown are comparisons of burst samples from Apertif and LOFAR (**a**), Apertif and CHIME/FRB (**b**), and CHIME/FRB and LOFAR (**c**). In all panels, the vertical grey dotted, dash-dotted and dashed lines show respectively the P value where 68.27% (1σ), 95.45% (2σ) and 99.73% (3σ) of the simulations give a larger P value.

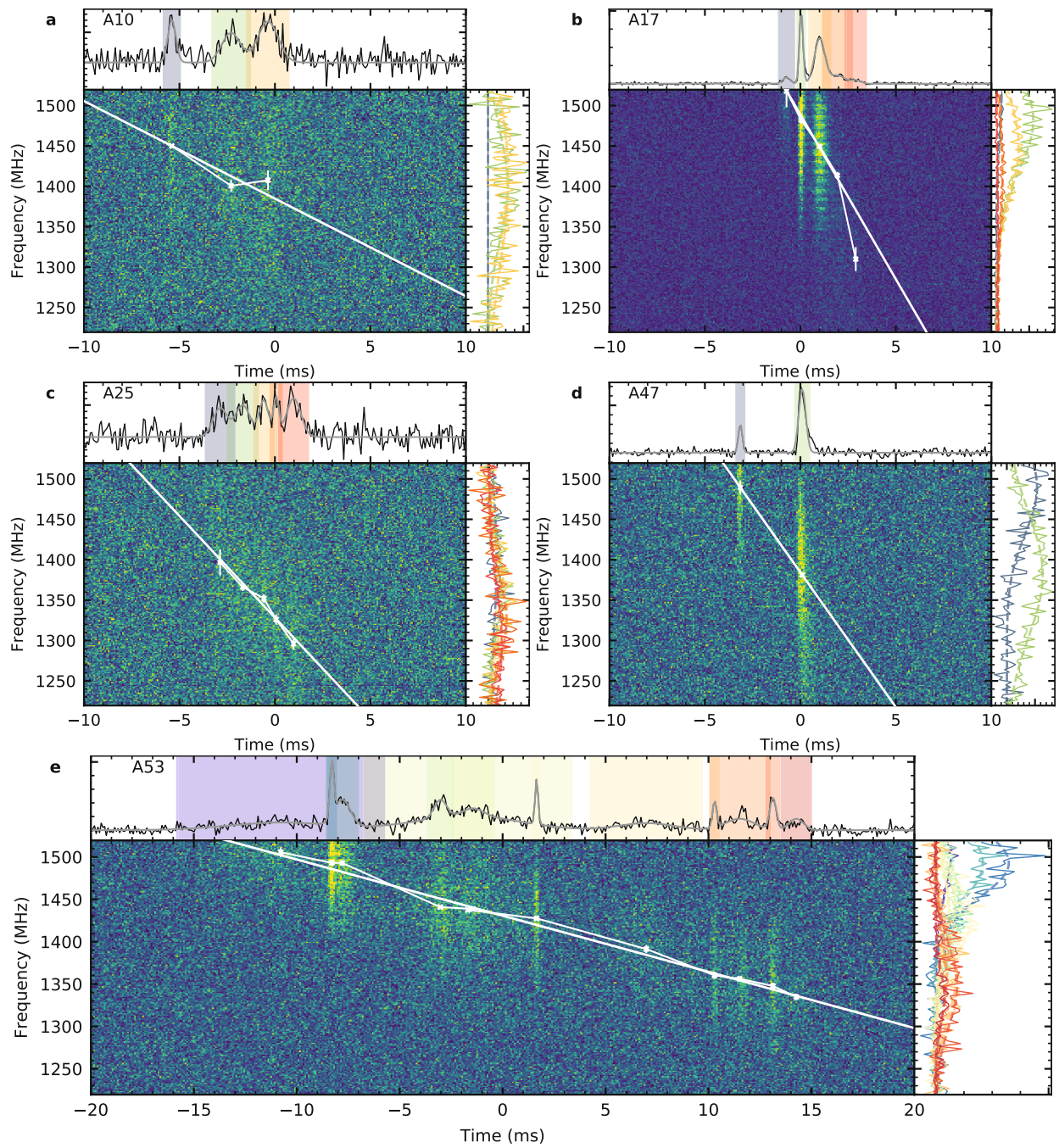


Extended Data Fig. 6 | Stacked LOFAR bursts. After dedispersion to the S/N-maximizing DM of $349.00 \text{ pc cm}^{-3}$, the individual bursts were co-added. **a**, The pulse profiles in eight different frequency bands of the co-added total, and fits to the scattering tail. The central frequency of the band is indicated on the vertical-axis labels. **b**, The dynamic spectrum of the stacked bursts.



Extended Data Fig. 7 | Apertif burst properties against phase. **a**, The structure-optimized DM, with the $348.75 \text{ pc cm}^{-3}$ average as a reference. **b**, The drift rate of bursts with multiple components. **c, d**, The fluence (**c**) and the average polarization position angle (**d**) of each burst. In all panels,

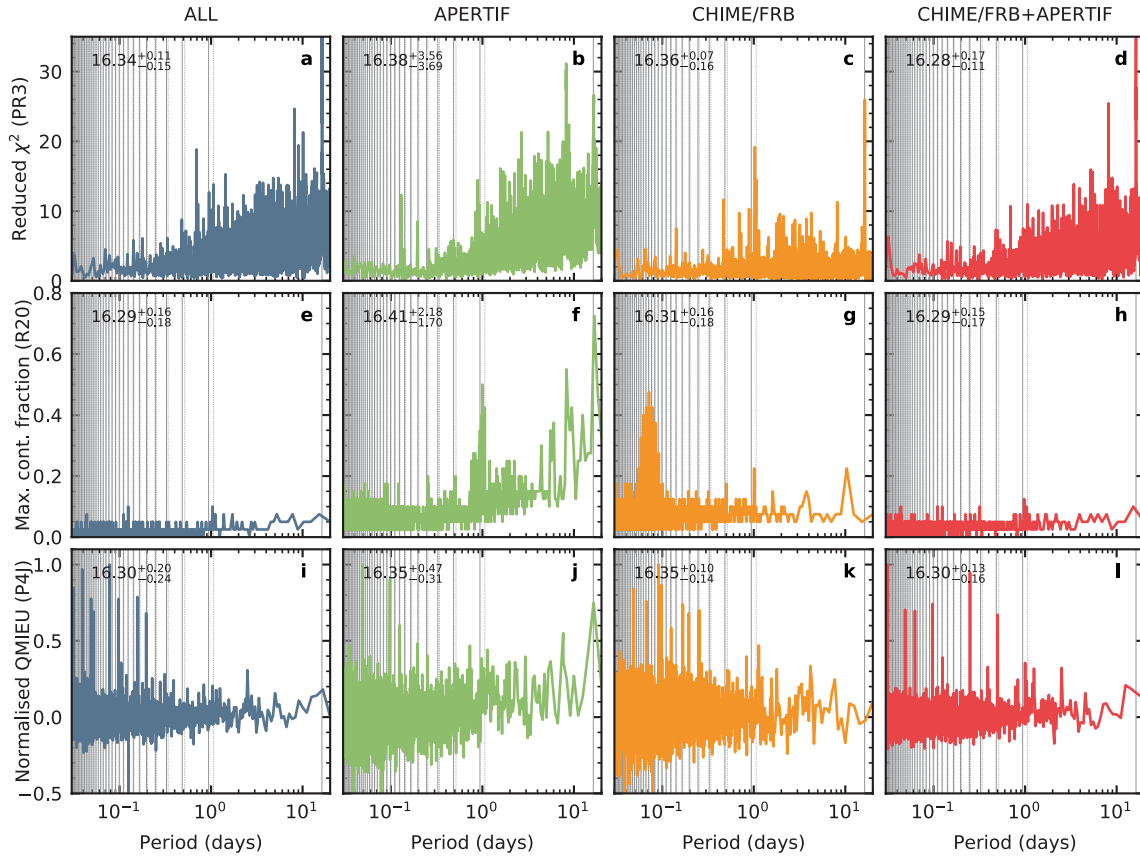
bursts are colour-coded by activity cycle. Each colour corresponds to a different activity cycle (see key at bottom left), and the data points with a black edge represent bursts with $S/N > 20$. The error bars represent 1σ (s.d.) errors.



Extended Data Fig. 8 | Five of the bursts with a measurable drift rate.

a–e, For each burst, the top panel shows the pulse profile as a solid black line and the fitted multi-component Gaussian in grey (the burst name is given at top left.). Coloured regions indicate the subcomponent position. The main panels

show the dynamic spectra, the subcomponent centroids with 1σ (s.d.) errors and the fitted drift rate \dot{v} (white line). The right panels display the spectra and the fitted Gaussian of each subcomponent, with the same colour as the shaded region of the pulse profile.



Extended Data Fig. 9 | Finding the best period. **a–l**, The periodograms between 0.03 day and 20 day periods of four instrument combinations and three different period searching techniques. Each column corresponds, from left to right, to all detections combined (blue), Apertif detections (green), CHIME/FRB detections (yellow) and CHIME/FRB and Apertif detections combined (red). Each row corresponds to a different search technique, with

Pearson's χ^2 test⁷ at the top, maximum continuous fraction in the centre²¹, and the normalized QMIEU method³⁴ at the bottom. The vertical grey lines mark the position of the aliased periods, solid lines for $f_N = (Nf_{\text{sid}} + f_0)$ and dotted lines for $f_N = (Nf_{\text{sid}} - f_0)$. The number in the top left corner of each plot indicates the best period using the given burst data set and periodicity search method, with errors giving the full-width at half-maximum.

Extended Data Table 1 | Summary of LOFAR burst properties

Burst ID	OBSID	Arrival time (MJD)	Arrival time (UTC)	Detection S/N	DM (pc cm ⁻³)	Fluence (Jy ms)	$\tau_{\text{sc}} \text{ at } 150 \text{ MHz}$ (ms)
L01	L775795	58949.53491816	2020-04-10 12:50:16.929	8.7	349.03±0.11	111±55	...
L02	L775801	58949.63987585	2020-04-10 15:21:25.273	7.3	348.94±0.08	38±19	...
L03	L775977	58950.52919335	2020-04-11 12:42:02.305	9.5	349.02±0.08	80±40	...
L04	L775977	58950.54130169	2020-04-11 12:59:28.466	18.9	349.41±0.03	177±88	...
L05	L775979	58950.58347838	2020-04-11 14:00:12.532	13.7	349.09±0.04	129±64	...
L06	L775953	58951.54162736	2020-04-12 12:59:56.604	29.4	349.03±0.05	318±159	48.2±16.6
L07	L775953	58951.55801455	2020-04-12 13:23:32.457	35.1	348.98±0.02	296±148	46.9±16.0
L08	L775955	58951.58470795	2020-04-12 14:01:58.767	23.5	348.99±0.03	193±96	36.2±19.0
L09	L775955	58951.59135120	2020-04-12 14:11:32.744	12.5	348.86±0.08	124±62	42.0±17.4

Article

Extended Data Table 2 | Summary of Apertif burst properties

Burst ID	Arrival time (MJD)	Arrival time (UTC)	Detection S/N	DM (pc cm ⁻³)	Fluence (Jy ms)	Drift rate (MHz ms ⁻¹)
A01	58930.47097294	2020-03-22T11:18:12.062	11.5	348.70(20)	1.8	...
A02	58931.51122577	2020-03-23T12:16:09.907	12.7	348.88(18)	6.2	...
A03	58931.54877968	2020-03-23T13:10:14.564	13.4	349.02(59)	8.0	...
A04	58931.56964778	2020-03-23T13:40:17.568	13.4	348.70(97)	4.2	-91.58
A05	58978.59561357	2020-05-09T14:17:41.012	13.6	348.63(14)	5.2	...
A06	58979.50785914	2020-05-10T12:11:19.030	8.9	348.35(38)	4.0	...
A07	58980.35572077	2020-05-11T08:32:14.275	16.4	348.75(26)	8.2	...
A08	58980.38590828	2020-05-11T09:15:42.475	29.9	349.44(26)	15.3	-10.82
A09	58980.44318898	2020-05-11T10:38:11.528	13.9	350.09(37)	1.7	...
A10	58980.46375074	2020-05-11T11:07:48.064	17.8	347.86(54)	14.2	-3.95
A11	58980.46995949	2020-05-11T11:16:44.500	10.1	347.28(32)	8.3	...
A12	58980.47426015	2020-05-11T11:22:56.077	11.0	349.06(33)	1.6	...
A13	58980.52593337	2020-05-11T12:37:20.643	38.6	348.70(56)	24.2	...
A14	58980.54629988	2020-05-11T13:06:40.310	14.0	348.07(44)	3.4	...
A15	58980.54684270	2020-05-11T13:07:27.209	12.5	349.52(76)	1.3	...
A16	58980.62542392	2020-05-11T15:00:36.627	11.5	348.78(48)	1.2	...
A17	58980.62998094	2020-05-11T15:07:10.353	58.1	348.68(13)	56.0	-37.62
A18	58980.65889322	2020-05-11T15:48:48.374	25.6	348.87(16)	18.6	-24.90
A19	58981.38138907	2020-05-12T09:09:12.016	31.5	350.68(32)	16.0	...
A20	58996.15501128	2020-05-27T03:43:12.975	12.1	348.81(21)	6.6	-27.74
A21	58996.19203445	2020-05-27T04:36:31.776	12.7	348.79(21)	3.7	-7.61
A22	58996.23898191	2020-05-27T05:44:08.037	20.2	348.68(14)	9.2	-13.91
A23	58996.27129126	2020-05-27T06:30:39.565	20.9	348.68(23)	5.5	-64.82
A24	58996.34499129	2020-05-27T08:16:47.247	21.4	350.23(84)	12.1	...
A25	58996.36224320	2020-05-27T08:41:37.812	19.5	348.78(44)	12.8	-24.51
A26	58996.42810299	2020-05-27T10:16:28.098	10.5	349.47(29)	2.0	...
A27	58996.48015176	2020-05-27T11:31:25.112	21.0	348.63(25)	3.2	...
A28	58996.60480633	2020-05-27T14:30:55.267	20.9	348.97(28)	8.4	-39.42
A29	58996.61583838	2020-05-27T14:46:48.436	9.0	348.81(43)	8.7	...
A30	58997.15492630	2020-05-28T03:43:05.632	25.7	348.87(22)	27.1	-18.10
A31	58997.23883623	2020-05-28T05:43:55.450	36.5	348.24(25)	17.6	...
A32	58997.26968437	2020-05-28T06:28:20.730	29.9	348.76(25)	14.0	...
A33	58997.35800780	2020-05-28T08:35:31.874	29.2	348.87(17)	13.8	...
A34	58997.38837259	2020-05-28T09:19:15.392	20.9	348.75(18)	3.5	...
A35	58998.15708057	2020-05-29T03:46:11.761	10.4	348.69(26)	5.8	...
A36	59095.01258701	2020-09-03T00:18:07.518	8.5	348.21(42)	17.7	...
A37	59095.01647024	2020-09-03T00:23:43.029	10.3	348.70(40)	7.2	...
A38	59095.03083630	2020-09-03T00:44:24.256	27.4	348.71(27)	7.5	-83.02
A39	59095.03119917	2020-09-03T00:44:55.608	28.2	348.73(11)	17.9	-94.55
A40	59095.04813576	2020-09-03T01:09:18.930	25.8	348.74(16)	4.2	...
A41	59095.06242878	2020-09-03T01:29:53.847	11.4	348.64(26)	5.3	...
A42	59095.07525644	2020-09-03T01:48:22.156	12.7	348.59(34)	3.1	...
A43	59095.07913932	2020-09-03T01:53:57.637	11.5	348.10(23)	2.5	...
A44	59095.10211216	2020-09-03T02:27:02.491	12.6	349.06(23)	4.2	...
A45	59095.11289895	2020-09-03T02:42:34.469	13.2	348.50(28)	3.5	...
A46	59095.11989684	2020-09-03T02:52:39.087	20.7	348.78(14)	7.1	...
A47	59095.12368446	2020-09-03T02:58:06.337	32.4	348.93(23)	11.2	-32.44
A48	59095.14075045	2020-09-03T03:22:40.839	10.0	349.14(51)	5.5	...
A49	59095.16236684	2020-09-03T03:53:48.495	10.7	349.29(26)	9.3	...
A50	59095.19030365	2020-09-03T04:34:02.235	9.4	349.68(52)	5.5	...
A51	59096.20840871	2020-09-04T05:00:06.513	9.3	348.43(54)	2.9	...
A52	59143.81778929	2020-10-21T19:37:36.995	11.3	348.89(19)	4.7	...
A53	59190.73164688	2020-12-07T17:33:34.290	44.2	348.76(19)	58.3	-6.55
A54	59191.74125466	2020-12-08T17:47:24.403	51.1	348.87(16)	20.4	-80.80